HD 28109 hosts a trio of transiting Neptunian planets including a near-resonant pair, confirmed by ASTEP from Antarctica

Dransfield, G.; Triaud, A.H.M.J.; Guillot, T.; Mekarnia, D.; Nesvorný, D.; Crouzet, N.M.; ... ; Zhou, G.

HD 28109 hosts a trio of transiting Neptunian planets including a near-resonant pair, confirmed by ASTEP from Antarctica

Georgina Dransfield,[1]* Amaury H.M.J. Triaud,[1] Tristan Guillot,[2] Djamel Mekarnia,[2] David Nesvorný,[3] Nicolas Crouzet,[4,5] Lyu Abe,[2] Karim Agabi,[2] Marco Buttu,[6] Juan Cabrera,[7] Davide Gandolfi,[8] Maximilian N. Günther[4]†, Florian Rodler,[9] François-Xavier Schmider,[2] Philippe Stee,[2] Olga Suarez,[2] Karen A. Collins,[10] Martín Dévora-Pajares,[11] Steve B. Howell,[12] Elisabeth C. Matthews,[13] Matthew R. Standing,[1] Keivan G. Stassun,[14] Chris Stockdale,[15] Samuel N. Quinn,[10] Carl Ziegler,[16] Ian J. M. Crossfield,[17] Jack J. Lissauer,[11] Andrew W. Mann,[18] Rachel Matson,[19] Joshua Schlieder,[20] George Zhou[21]

[1]*School of Physics & Astronomy, University of Birmingham, Edgbaston, Birmingham B15 2TT, United Kingdom*
[2]*Université Côte d'Azur, Observatoire de la Côte d'Azur, CNRS, Laboratoire Lagrange, Bd de l'Observatoire, CS 34229, 06304 Nice cedex 4, France*
[3]*Southwest Research Institute, Department of Space Studies 1050 Walnut St., Suite 400, Boulder, Colorado 80302*
[4]*European Space Agency (ESA), European Space Research and Technology Centre (ESTEC), Keplerlaan 1, 2201 AZ Noordwijk, The Netherlands*
[5]*Leiden Observatory, Leiden University, Postbus 9513, 2300 RA, Leiden, The Netherlands*
[6]*INAF OAS, Osservatorio di Astrofisica e Scienza dello Spazio di Bologna via Piero Gobetti 93/3, Bologna, Italy*
[7]*Deutsches Zentrum für Luft- und Raumfahrt, Rutherfordstr. 2, D-12489 Berlin, Germany*
[8]*Dipartimento di Fisica, Università Degli Studi di Torino Via Pietro Giuria, 1, 10125, Torino, Italia*
[9]*European Southern Observatory, Alonso de Cordova 3107, Vitacura, Santiago, Chile*
[10]*Center for Astrophysics | Harvard & Smithsonian, 60 Garden St, Cambridge, MA 02138, USA*
[11]*Dpto. Física Teórica y del Cosmos, Universidad de Granada, 18071, Granada, Spain*
[12]*NASA Ames Research Center, Moffett Field, CA 94035, USA*
[13]*Geneva Observatory, University of Geneva, Chemin Pegasi 51, 1290 Versoix, Switzerland*
[14]*Department of Physics & Astronomy, Vanderbilt University, 6301 Stevenson Center Ln., Nashville, TN 37235, USA*
[15]*Hazelwood Observatory*
[16]*Department of Physics, Engineering and Astronomy, Stephen F. Austin State University, 1936 North St, Nacogdoches, TX 75962, USA*
[17]*Department of Physics and Astronomy, University of Kansas, Lawrence, KS, USA*
[18]*Department of Physics and Astronomy, The University of North Carolina at Chapel Hill, Chapel Hill, NC 27599-3255, USA*
[19]*The United States Naval Observatory, 3450 Massachusetts Ave, NW, Washington, DC 20392-5420*
[20]*NASA Goddard Space Flight Center, 8800 Greenbelt Rd, Greenbelt, MD 20771, United States*
[21]*Centre for Astrophysics, University of Southern Queensland, West Street, Toowoomba, QLD 4350, Australia*

ABSTRACT

We report on the discovery and characterisation of three planets orbiting the F8 star HD 28109, which sits comfortably in *TESS*'s continuous viewing zone. The two outer planets have periods of 56.0067 ± 0.0003 days and $84.2597^{+0.0010}_{-0.0008}$ days, which implies a period ratio very close to that of the first-order 3:2 mean motion resonance, exciting transit timing variations (TTVs) of up to 60 mins. These two planets were first identified by *TESS*, and we identified a third planet in the *TESS* photometry with a period of 22.8911 ± 0.0004 days. We confirm the planetary nature of all three planetary candidates using ground-based photometry from *Hazelwood*, *ASTEP* and *LCO*, including a full detection of the ~ 9 h transit of HD 28109 c from Antarctica. The radii of the three planets are $R_b = 2.199^{+0.098}_{-0.10}\ R_\oplus$, $R_c = 4.23 \pm 0.11\ R_\oplus$ and $R_d = 3.25 \pm 0.11\ R_\oplus$; we characterise their masses using TTVs and precise radial velocities from ESPRESSO and HARPS, and find them to be $M_b = 18.5^{+9.1}_{-7.6}\ M_\oplus$, $M_c = 7.9^{+4.2}_{-3.0}\ M_\oplus$ and $M_d = 5.7^{+2.7}_{-2.1}\ M_\oplus$, making planet b a dense, massive planet while c and d are both under-dense. We also demonstrate that the two outer planets are ripe for atmospheric characterisation using transmission spectroscopy, especially given their position in the CVZ of *JWST*. The data obtained to date are consistent with resonant (librating) and non-resonant (circulating) solutions; additional observations will show whether the pair is actually locked in resonance or just near-resonant.

Key words: planets and satellites: detection – planets and satellites: dynamical evolution and stability – planets and satellites: fundamental parameters

* gd@bham.ac.uk †ESA Research Fellow

1 INTRODUCTION

The discovery of over 4 500 extrasolar planets has in no way diminished our curiosity regarding our place in the universe; if anything, we have more questions than ever.

Following early results by Doppler surveys (e.g. Mayor et al. 2011; Howard et al. 2010b), the *Kepler* survey (Borucki et al. 2010) revealed an abundant population of planets comparable in size to Neptune (Fressin et al. 2013), the majority occupying periods shorter than a few hundred days (Howard et al. 2010a). The formation of these Neptune-size worlds remains debated; one possible pathway is that 'pebbles' (large dust particles) separate from the gas in the planet-forming disc and drift inward (Johansen & Lambrechts 2017). Another possibility is that the pebbles are accreted into cores before migrating inward (Coleman & Nelson 2016); thus both models predict that most of the mass growth takes place in situ (e.g. Lambrechts et al. 2019; Bean et al. 2021).

Both the 'drift' and 'migration' formation pathways predict the formation of resonant chains, where adjacent planets find themselves in a mean-motion resonance with their neighbours (Bean et al. 2021). However most planets are not found with commensurate orbital periods (Fabrycky et al. 2014). Studies show that in ~95% of cases the resonance chain becomes unstable following the dispersal of the gas disc (Matsumura et al. 2010; Pu & Wu 2015; Izidoro et al. 2021). Alternatively, the migratory pathway might be more chaotic (Rein 2012; Lee & Chiang 2015).

Statistical studies of the large samples of known planets have shown that multiplicity is common, i.e. many planets are in multiplanet systems (Fabrycky et al. 2014). Those planets that find themselves close to a mean-motion resonance with their neighbours allow for masses to be constrained without spectroscopic follow-up, by monitoring transit timing variations (TTVs) in the system (e.g. Agol et al. 2005; Holman & Murray 2005; Holman et al. 2010; Lithwick et al. 2012).

Neptune-sized planets orbiting bright stars provide excellent dynamical laboratories to further investigate these exciting systems. *TESS*, the Transiting Exoplanet Survey Satellite (Ricker et al. 2015) launched in 2018 to search for exoplanet candidates; one of its primary mission aims is to deliver to the community 50 planets smaller than 4 $R_\oplus$, with masses measured by high precision radial velocity (RV). Not all systems are suitable for RV mass measurements, but it is predicted that *TESS* will also observe ∼ 30 systems with TTVs, with approximately a third of those being suitable for dynamical mass measurements (Hadden et al. 2019). Another of *TESS*'s goals is the identification of planets orbiting bright stars, to permit detailed investigations into the dynamics and chemical composition of exoplanetary atmospheres. The discovery and analysis of HD 28109 (TOI-282) fulfils two of those primary objectives.

Stars within *TESS*'s northern and southern continuous viewing zones (CVZ) are continuously observed for a year, allowing for the discovery of long period planets (> 20 days). These planets are likely to be favourable candidates for *JWST* as its CVZ falls within *TESS*'s; however they are challenging to confirm with ground-based photometry, especially if TTVs introduce large timing uncertainties.

Unless, of course, one is observing from Antarctica. *ASTEP* (**A**ntarctic **S**earch for **T**ransiting **Exo****P**lanets Guillot et al. 2015; Mékarnia et al. 2016) is a 40 cm telescope located on the Antarctic Plateau at a latitude of −75.1 deg an elevation of 3, 233 m. This unique location has a thin atmosphere, completely dry air, and virtually uninterrupted observing between late May and late July (Crouzet et al. 2010a,b). The visibility covers *TESS*'s CVZ and the area where Low-Earth Orbit telescopes have trouble reaching (e.g. CHEOPS

Broeg et al. 2013). For this reason, *ASTEP* is the observatory (ground or space) best suited for the photometric confirmation and follow-up of long-period transiting systems.

In this work we present the discovery, validation and characterisation of three sub-Neptunes orbiting HD 28109. We begin by characterising the host in Section 2, followed by Sections 3 and 4 where we describe the identification and validation of planetary candidates in the system. In Section 5 we describe our global analysis of all available photometric and radial velocity data to characterise the planets. We then place the three planets in the context of the field, including potential for atmospheric characterisation of the system and further high precision radial velocity follow-up in Section 6. Finally, we summarise our findings and conclude in Section 7.

2 STELLAR CHARACTERISATION

HD 28109 (TOI-282) is a bright (V=9.42; J = 8.476) main-sequence star, of spectral type F8/G0V. Its right ascension and declination are 04:20:57.19 -68:06:09.68, and it has a parallax of 7.13 mas (Gaia Collaboration et al. 2021, 2016), placing it at a distance of 140 pc (Bailer-Jones et al. 2021).

All planetary measurements are derived from our knowledge of the star; we therefore begin by characterising the radius, mass, effective temperature and spectral type of the star.

2.1 Reconnaissance Spectroscopy

We observed TOI-282 on three nights spanning 2019 February 14 to 2021 January 07 with the CHIRON spectrograph on the 1.5 m SMARTS telescope. CHIRON is a high resolution echelle spectrograph fed by an image slicer and a fiber bundle, located at Cerro Tololo Inter-American Observatory (CTIO), Chile. The spectra have a resolution of R = 80000 with a wavelength coverage of $4500 - 8900$ Å (Tokovinin et al. 2013). The wavelength solution is provided by bracketing Thorium-Argon cathode-ray lamp observations, and the spectra are extracted and wavelength calibrated with the official CHIRON pipeline (Paredes et al. 2021). We extracted the RVs by fitting the spectral line profiles, which were measured via least-squares deconvolution of the observed spectra using synthetic templates (Donati et al. 1997). The three RVs exhibit a root mean square scatter of $58\,m/s$, which is not significant given the $44\,m/s$ mean per-point uncertainty. With these data, we cannot place strong limits on the presence of additional companions, but the two-year time span of the observations does allow us to measure long-term trends that might be indicative of very massive outer companions. The best-fit linear trend $(0.076 \pm 0.091\,m/s/day)$ is consistent with zero, which suggests it is unlikely that there is a stellar companion in the system, but the precise radial velocities described in Section 4.3 can provide tighter constraints on the masses of the transiting planets and limits on the presence of other bound companions.

We also use the CHIRON spectra to determine the effective temperature, surface gravity, and metallicity of the host star by matching against observed spectra that have previously been classified using SPC (Buchhave et al. 2012). Interpolation to the final parameters is performed with a gradient-boosting regressor implemented in the SCIKIT-LEARN python module. We measure $T_{\rm eff} = 6120 \pm 50$ K, $\log g_\star = 4.13 \pm 0.10$, and [Fe/H] $= 0.0 \pm 0.10$. Following Gray (2005) and Zhou et al. (2018), we derive $v \sin i_\star$ by fitting broadening kernels to the instrumental, macroturbulent, and rotational line profiles, and estimate $v \sin i_\star = 7.7 \pm 0.5\,km\,s^{-1}$.
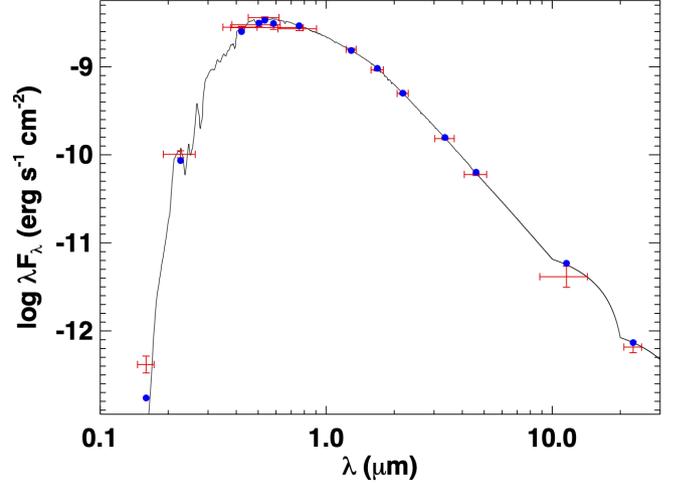

Figure 1. Spectral energy distribution (SED) of TOI-282. Red symbols represent the observed photometric measurements, where the horizontal bars represent the effective width of the passband. Blue symbols are the model fluxes from the best-fit Kurucz atmosphere model (black).

2.2 Spectral Energy Distribution

As an independent check on the derived stellar parameters, and in order to determine an estimate for stellar age, we perform an analysis of the broadband spectral energy distribution (SED). Together with the *Gaia* EDR3 parallax, we determine an empirical measurement of the stellar radius following the procedures described in Stassun & Torres (2016); Stassun et al. (2017, 2018). We pulled the $B_T V_T$ magnitudes from *Tycho-2*, the JHK_S magnitudes from *2MASS*, the W1–W4 magnitudes from *WISE*, and the $GG_{\rm RP}G_{\rm BP}$ magnitudes from *Gaia*. In addition, we pulled the FUV and NUV fluxes from *GALEX* in order to assess the level of chromospheric activity, if any. Together, the available photometry spans the full stellar SED over the wavelength range 0.2–22 μm (see Figure 1).

We perform a fit using Kurucz stellar atmosphere models (Kurucz 1979), with the effective temperature ($T_{\rm eff}$) and metallicity ([Fe/H]) adopted from the spectroscopic analysis. The remaining free parameter is the extinction, A_V, which was limited to the maximum line-of-sight value from the dust maps of Schlegel et al. (1998). The resulting fit is very good (Figure 1) with a best-fit $A_V = 0.01 \pm 0.01$ and a reduced χ^2 of 2.8 (excluding the *GALEX* FUV flux, which is consistent with a modest level of chromospheric activity; see below). Integrating the (unreddened) model SED gives the bolometric flux at Earth of $F_{\rm bol} = 4.37 \pm 0.15 \times 10^{-9}$ erg s^{-1} cm^{-2}. Taking the $F_{\rm bol}$ and $T_{\rm eff}$ together with the *Gaia* EDR3 parallax, with no systematic offset applied (see, e.g., Stassun & Torres 2021), gives the stellar radius as $R_\star = 1.446 \pm 0.035$ R$_\odot$. Finally, estimating the stellar mass from the empirical relations of Torres et al. (2010) and a 6% error from the empirical relation itself gives $M_\star = 1.26 \pm 0.08$ M$_\odot$, consistent with the mass estimated empirically from the stellar radius together with the spectroscopic $\log g$ which gives $M_\star = 1.03 \pm 0.24$ M$_\odot$.

We can also estimate the stellar age by taking advantage of the observed modest chromospheric activity in the UV together with empirical age-activity-rotation relations. For example, we can estimate the $\log R'_{\rm HK} = -4.56 \pm 0.05$ via the *GALEX* FUV excess and the empirical relations of Findeisen et al. (2011). That implies an age of $\tau = 0.9 \pm 0.3$ Gyr via the empirical activity-age relations of Mamajek & Hillenbrand (2008). Finally, we can further corroborate the activity-based age estimate by also using empirical relations to predict the stellar rotation period from the activity. For example, the

Designations	HD 28109, TIC 29781292, TOI-282, 2MASS J04205712-6806095, UCAC4 110-003794, WISE J042057.17-680609.5, Gaia DR2 4668163021600295552, HIP 20295, TYC 9154-01248-1	
Parameter	**Value**	**Source**
T mag	8.9387±0.006	Stassun et al. (2019)
B mag	9.91±0.03	Høg et al. (2000)
V mag	9.38±0.02	Høg et al. (2000)
G mag	9.3063±0.0028	Gaia Collaboration et al. (2021)
J mag	8.476±0.020	Cutri et al. (2003)
H mag	8.256±0.024	Cutri et al. (2003)
K mag	8.175±0.023	Cutri et al. (2003)
W1 mag	8.136±0.023	Wright et al. (2010)
W2 mag	8.175±0.020	Wright et al. (2010)
W3 mag	8.155±0.020	Wright et al. (2010)
W4 mag	7.997±0.161	Wright et al. (2010)
Distance	140.087±0.194	Bailer-Jones et al. (2021)
SpT	F8/G0V	Houk & Cowley (1975)
$R_\star$	$1.446 \pm 0.035 R_\odot$	This work
$M_\star$	$1.26 \pm 0.08 M_\odot$	This work
Age	1.1±0.1 Gyr	This work
T_{eff}	6120±50 K	This work
$\log g_\star$	4.13±0.10	This work
[Fe/H]	0.0±0.1	This work
$v \sin i_\star$	7.7±0.5 km/s	This work

Table 1. Stellar parameters adopted for this work.

empirical relation between R'_{HK} and rotation period from Mamajek & Hillenbrand (2008) predicts a rotation period for this star of 7.2 ± 1.1 d, which is compatible with the (projected) rotation period $P_{rot}/\sin i_\star = 9.51 \pm 0.62$ d inferred from the stellar radius above together with the spectroscopic $v \sin i_\star$.

We present the adopted stellar parameters in Table 1.

3 IDENTIFICATION OF PLANETARY CANDIDATES

HD 28109 (TOI-282) is in the southern continuous viewing zone (CVZ) for *TESS* which means it is observed in all southern sectors, the only exception being sector 32 where the target was off the edge of the CCD by 3 pixels. At the time of writing, the star has been observed in 25 sectors at two-minute cadence.

In the following sections we describe the identification of candidates by *TESS*, as well as our own search for further candidates in the data.

3.1 Note on Nomenclature

Throughout Section 3 we refer to the host (HD 28109) using its *TESS* alias: TOI-282, where TOI is *TESS* Object of Interest. When referring to candidate planets, we also use the *TESS* nomenclature and add numeric suffixes in the order that candidates were identified. Once the candidates are confirmed we change their names. Thus, TOI-282.01 becomes HD 28109 c; TOI-282.03 becomes HD 28109 d; and TOI-282.04 is HD 28109 b, with letters indicating the order from closest to farthest from the host star.

3.2 *TESS* data

All 2 minute cadence *TESS* data is reduced by the SPOC (Science Processing Operations Center) pipeline (Jenkins et al. 2016) and

the photometry data products are delivered in the form of simple aperture photometry (SAP) or Presearch Data Conditioning Simple Aperture Photometry (PDCSAP), where the latter has been corrected for instrument systematics. The lightcurves are then searched for transit-like signals; candidates that have a signal-to-noise ratio ≥ 7 are reported as threshold crossing events (TCEs).

The first TCE on TOI-282 was detected in Sector 1, and a second was detected in Sector 2. The multi-sector data validation report for Sectors 1-2 showed this as a planetary candidate with a period of ~18 days. It wasn't until Sectors 1-6 were available that the individual candidates could be disentangled. The 1–6 multi-sector validation report reported three planet candidates on TOI-282: candidate .01 with a period of ≈56 days, .02 with a period of ≈31 days, and finally .03 with a period of ≈84 days. Candidate .02 was later retired as a false alarm[1].

The PDCSAP lightcurves for Sectors 1-13 and Sectors 27-39 can be found in Figure 2, where transits of TOI-282.01 are highlighted in yellow, while the transits of TOI-282.03 are in green.

3.3 Search For Additional Transiting Candidates

We made use of the custom SHERLOCK[2] pipeline presented in Pozuelos et al. (2020) and Demory et al. (2020) to perform a search for additional transiting candidates in the *TESS* data. SHERLOCK uses the LIGHTKURVE package (Lightkurve Collaboration et al. 2018) to download *TESS* PDCSAP data from NASA Mikulski Archive for Space Telescope (MAST); any outliers, defined as any points over 3σ above the running mean, are then removed. The pipeline then uses WOTAN (Hippke et al. 2019) to detrend the data using the biweight method testing several window lengths. In this case, we used six window sizes between 0.64 and 3.55 days in order to optimise signal detection efficiency (SDE). To aid in the detection of low SNR signals, SHERLOCK also optionally applies a a Savitzky–Golay filter (Savitzky & Golay 1964) to smooth the data and increase precision.

The search for periodic signals is carried out using the TRANSIT LEAST SQUARE (TLS) package (Hippke & Heller 2019) as it is optimised to search for periodic signals with transit-like shapes. We searched a wide parameter space, with periods ranging from 5 to 100 days setting the minimum signal-to-noise ratio (SNR) to 5. This is in contrast to the SPOC pipeline, which sets the minimum SNR to 7.

We recover both candidates .01 and .03 in the first instance and find that the SDE is consistent across all window sizes, although the SNR and transit depths are at their highest using a window size of 2.8259 days. We also find a third significant signal at a period of 22.89±0.01 days. This signal has an SNR of 23.8 and SDE of 13.1 using the same window-size as for the first two candidates; its depth of just 0.14ppt (parts per thousand) would make it extremely challenging to detect from the ground. Nevertheless, if this is indeed a third planet in the system, its size would be classed as a mini-Neptune just beyond the so-called radius valley (Fulton et al. 2017; Van Eylen et al. 2018), and its period would place it within ~ 5% of a 5:2 third order resonance with candidate .01. The *TESS* lightcurve folded on this signal is presented in Figure 3, along with the Lomb-Scargle periodogram.

While this signal does not match any of the TOIs on ExoFOP, further scrutiny reveals that this might have been the period originally associated with TOI-282.02. Dietrich & Apai (2020) include the

---

[1] The 31-day transit event was caused by a combination of noise and confusion with the 84-day transit events in early TESS data.

[2] SHERLOCK is publicly available at https://github.com/franpoz/SHERLOCK.
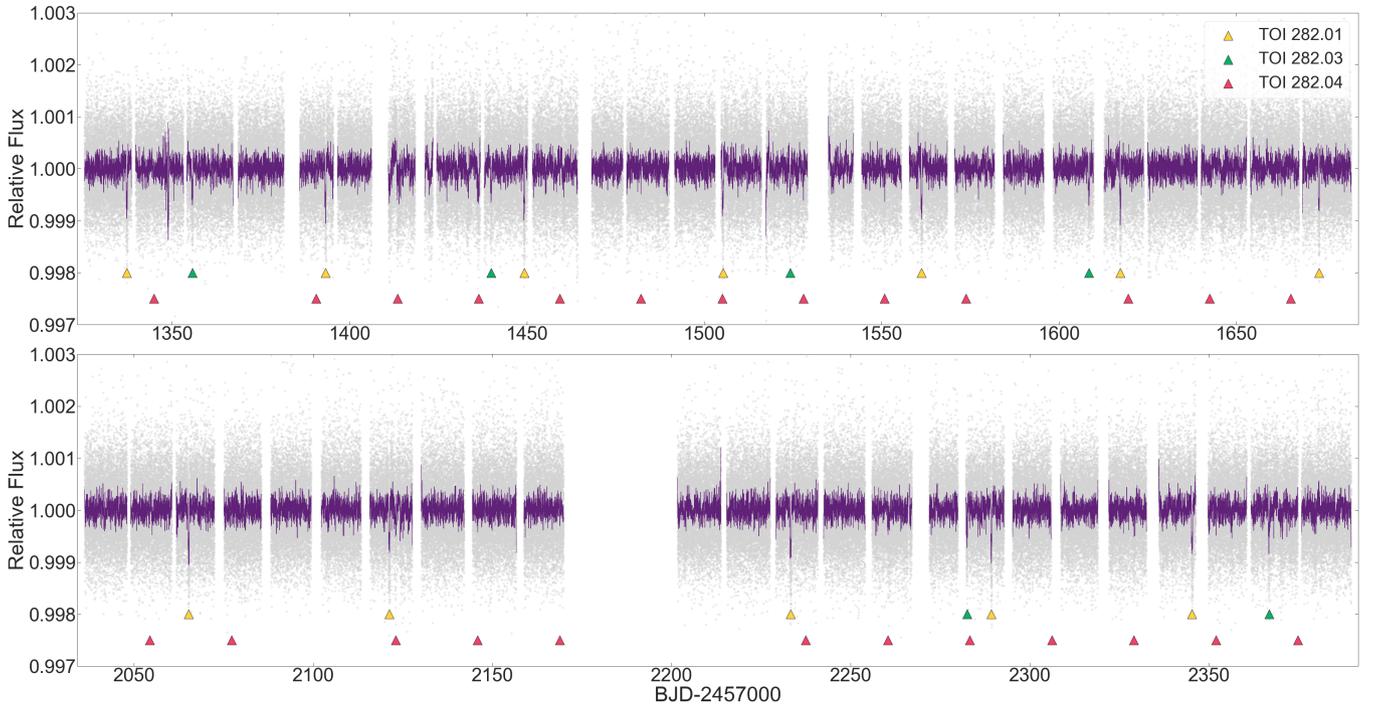
Figure 2. PDCSAP lightcurves of TOI-282, as produced by the SPOC pipeline. The top panel shows the photometry for sectors 1-13, while the bottom panel contained sectors 27-37, with a gap where sector 32 was missing. Binned data with a cadence of 30 min are shown in purple.

candidates of TOI-282 in their sample, and cite the orbital period for the innermost candidate as $\sim$ 22.89 days. Additionally, when we scrutinise some of the first multi-sector data validation reports produced by the SPOC pipeline, we find that Candidate 2 has a period of $\sim$ 22.89 days[3].

We now adopt this re-identified candidate as TOI-282.04 and indicate in dark pink the detected transits on Figure 2.

Two other periodic signals with low significance were also recovered which did not pass our vetting tests and are therefore attributed to instrument systematics.

4 VETTING AND VALIDATION OF CANDIDATES

In this section we describe first the ground-based follow-up observations we conducted, staring with high-resolution imaging of the host to search for blended companions. We then describe the photometric observations conducted from several sites between January 2019 and August 2021. In the first instance, the purpose of ground-based follow-up is to validate the planetary nature of the candidates; in Section 4.4 we describe how we used the available data on this system to rule out all feasible false positive scenarios.

We note that while the validation tests described here allowed us to confirm the planetary nature of TOI-282.01, .03 and .04 initially, the analysis we describe in Section 5.2 reveals anti-correlated transit timing variations between planets .01 and .03. Therefore, many of the tests here described are not necessary to validate these two objects as planets since TTVs are not known to have astrophysical false-positives. We nevertheless kept the validation steps here for completeness.

All follow-up observations are summarised in Table 2.

4.1 High Resolution Imaging

If an exoplanet star has a close companion (bound or line of sight), "third-light" flux from the companion can lead to an underestimated planetary radius if not accounted for in the transit modelling (Ciardi et al. 2015; Furlan & Howell 2017; Matson et al. 2018).

4.1.1 Gemini South Telescope

To search for close-in (bound) companions unresolved in other follow-up observations, we obtained high-resolution imaging observations from Gemini South's Zorro speckle interferometric instrument[4].

TOI-282 was observed using Zorro on UT 2020 December 23. Zorro provides simultaneous high-resolution speckle imaging in two optical bands, 562/54 and 832/40 nm, with output data products including a reconstructed image, and robust limits on companion detections (Howell et al. 2011, 2021). Figure 4 (upper panel) shows our 5σ detection limit contrast curves and the corresponding reconstructed speckle image in 832 nm. We find that TOI-282 is a single star with no companions detected in our observations down to a contrast level of 5 to 8 magnitudes from the Gemini 8-m diffraction limit out to 1.2". At the distance of TOI-282 (d=140 pc) these angular limits correspond to spatial limits of 2.8 to 168 AU.

---

[3] All data validation reports for TOI-282 are publicly available at https://exofop.ipac.caltech.edu/tess/target.php?id=29781292.

[4] https://www.gemini.edu/sciops/instruments/alopeke-zorro/

Table 2. Summary of ground-based follow-up observations carried out for the validation of TOI-282.01, .03 and .04.

Follow-up Observations				
High Resolution Imaging				
Observatory	**Filter**	**Date**	**Sensitivity Limit**	**Result**
VLT	K_s	2019 January 25	$\Delta m = 5$ at $0.23 - 4.5$"	No sources detected
SOAR	I_c	2019 February 02	$\Delta m = 7.3$ at $1 - 3$"	No sources detected
Gemini South	562 nm	2020 December 23	$\Delta m = 5$ at $0.1 - 1.2$"	No sources detected
Gemini South	832 nm	2020 December 23	$\Delta m = 8$ at $0.1 - 1.2$"	No sources detected
Photometric Follow-up				
Observatory	**Filter**	**Date**	**Coverage**	**Result**
TOI-282.01 / HD 28109 c				
Hazelwood	I_c	2019 January 19	Ingress +50%	Field cleared of NEBs within 2.5"
ASTEP	R_c	2020 June 08	Full	Detection
ASTEP	R_c	2021 March 15	Ingress +50%	Detection
ASTEP	R_c	2021 May 10	Ingress +90%	Detection
ASTEP	R_c	2021 July 05	Full	Non-detection
ASTEP	R_c	2021 August 30	Full	Non-detection
LCO	z_s	2021 August 30	Full	Field cleared of NEBs within 2.5"
TOI-282.03 / HD 28109 d				
ASTEP	R_c	2021 March 08	Ingress +30%	Field cleared of NEBs within 2.5"
ASTEP	R_c	2021 August 23	Ingress +40%	Field cleared of NEBs within 2.5"
TOI-282.04 / HD 28109 b				
Hazelwood	I_c	2019 January 19	Ingress +50%	Field cleared of NEBs within 2.5"
Spectroscopic Observations				
Instrument	**Wavelength Range**	**Date Range**	**Number of Spectra**	**Use**
CHIRON	$450 - 890$ nm	2019 February 14 - 2021 January 07	3	Stellar characterisation
ESPRESSO	$380 - 788$ nm	UT 2019 October 15 - UT 2019 December 27	8	Rule out stellar companion
HARPS	$383 - 693$ nm	UT 2019 May 24 - UT 2021 January 29	7	Rule out stellar companion

4.1.2 Southern Astrophysical Research Telescope

We also searched for stellar companions to TOI-282 with speckle imaging on the 4.1-m Southern Astrophysical Research (SOAR) telescope (Tokovinin 2018) on UT 2019 February 2, observing in Cousins I-band, a similar visible bandpass as *TESS*. This observation was sensitive to a 7.3-magnitude fainter star at an angular distance of 1 arcsec from the target. More details of the observation are available in Ziegler et al. (2020). The 5σ detection sensitivity and speckle auto-correlation functions from the observations are shown in Figure 4 (middle panel). No nearby stars were detected within $3''$of TOI-282 in the SOAR observations.

4.1.3 VLT NaCo

We collected high-resolution AO images of TOI-282 with VLT/NaCo (Lenzen et al. 2003; Rousset et al. 2003) on UT 2019 January 25, using the K_s filter. We collected 9 frames, each with exposure time 20s, and dithered the telescope by 2" in a grid-like pattern between each frame, and constructed a sky background frame by median combining the science images. We processed the data using a custom pipeline which corrects bad pixels, subtracts the sky frame and applies a flat-field correction, and then aligns the stellar position between each frame and co-adds the images. To test the sensitivity of these images, we injected faint fake PSFs into the data, and scaled them such that they could be redetected at 5σ. Significances are averaged radially and presented in Figure 4 (lower panel); the data are sensitive to companions 5mag fainter than the star beyond 230mas, and to companions 7mag fainter than the star in the back-

ground limited regime. We searched for companions in the reduced images by eye. Detector persistence at the dither positions causes a faint point source 2" directly to the south of the companion, but by inspecting the individual images we confirm that this is not a true visual companion. Apart from this persistence, no point sources are seen anywhere in the field of view, and we confirm that the star is single to the limit of our resolution.

4.2 Photometric Follow-up

Both candidates identified by *TESS* (TOI-282.01 and .03) have long periods (~ 56 d and ~ 84 d), long transit durations (> 8 h), and their transits are shallow. These constraints combined made TOI-282 a challenging system to follow-up from the ground, accounting for why the .01 only has seven photometric follow-up observations to date with three detections, while the .03 candidate has two observations with no transit detections.

Below we describe first the observations carried out by *Hazelwood*, followed by the observations taken by *ASTEP* and *LCO*.

4.2.1 Hazelwood

The *Hazelwood* Observatory is a backyard observatory with a 0.32 m Planewave CDK telescope working at f/8, a SBIG STT3200 2.2k $\times$ 1.5k CCD, giving a $20' \times 13'$ field of view and $0.55''$ per pixel. The camera is equipped with B, V, Rc, Ic, g', r', i' and z' filters. Typical FWHM is 2.2" to 2.7". The Hazelwood Observatory, operated by Chris Stockdale in Victoria, Australia, observed an ingress of TOI-282.01 in Ic on UT 2019 January 21; the transit was below
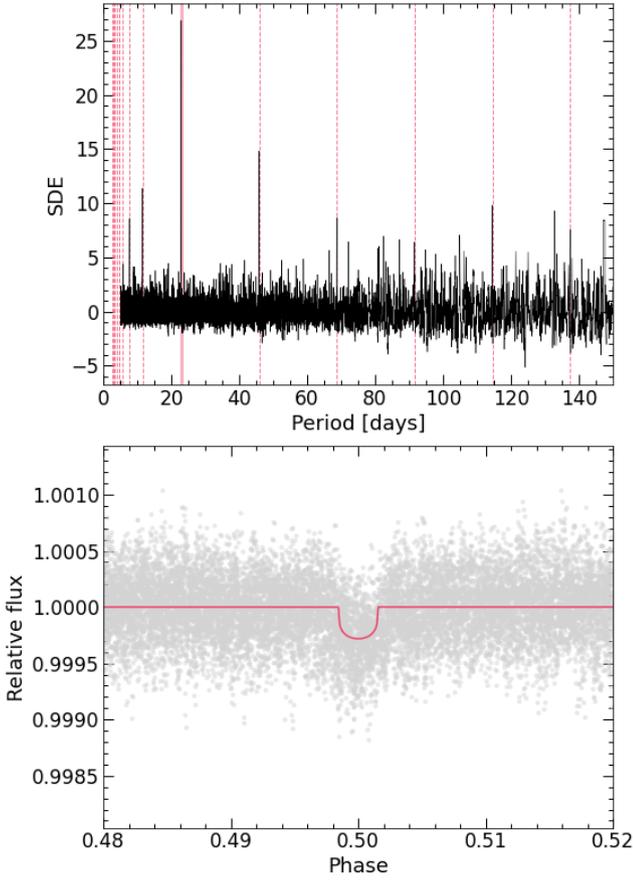
Figure 3. Results of our search for additional candidates in the data, using TRANSITLEASTSQUARES as implemented by SHERLOCK. **Upper panel:** Lomb-Scargle periodogram showing the detected period and its harmonics. **Lower panel:** *TESS* lightcurve phase-folded on this period, with a transit model overplotted.

the detection threshold, resulting in a flat lightcurve, but a nearby eclipsing binary (NEB) check cleared the field within 2.5′.

Coincidentally, this observation spanned a rare double transit that included the innermost candidate (TOI-282.04) as well. The successful NEB check therefore also applies to this candidate, ruling out nearby stars as the source of the event.

4.2.2 ASTEP

ASTEP is a custom 0.4 m Newtonian telescope equipped with a 5-lens Wynne coma corrector and a 4k × 4k front-illuminated FLI Proline KAF-16801E CCD. The camera has an image scale of 0.″93 pixel^{-1} resulting in a $1^o \times 1^o$ corrected field of view. The focal instrument dichroic plate splits the beam into a blue wavelength channel for guiding, and a non-filtered red science channel roughly matching an R_c transmission curve (Abe et al. 2013; Guillot et al. 2015). The telescope is automated or remotely operated when needed. Due to the extremely low data transmission rate at the Concordia Station, the data are processed on-site using an automated IDL-based aperture photometry pipeline (Mékarnia et al. 2016). The calibrated light curve is reported via email and the raw light curves of about 1,000 stars of the field are transferred to Europe on a server in Roma, Italy and are then available for deeper analysis. These data files contain
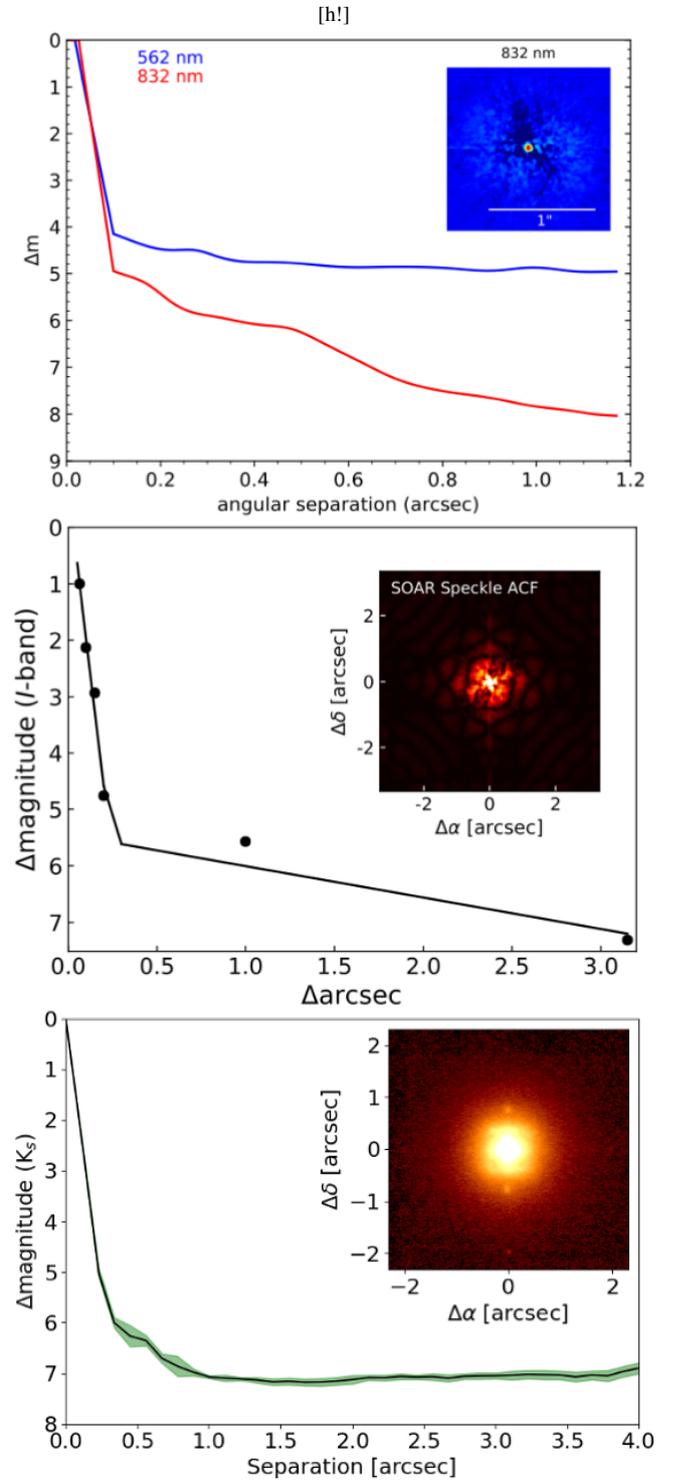
Figure 4. Contrast curves for HD 28109/TOI-282. The top panel shows the results from Gemini South, the middle panel shows the results from SOAR, and the bottom panel shows results from VLT/NaCo. All three panels are inset with final reconstructed images; none of the observations revealed bound companions within 5 magnitudes of the target.

each star's flux computed through 10 fixed circular apertures radii, so that optimal light curves can be extracted.

The *ASTEP* location at Dome C, on the Antarctic plateau, means that it enjoys excellent photometric conditions and exceptionally long nights (Crouzet et al. 2018). *ASTEP* is therefore well placed to observe targets with long orbital periods and transit durations.

We observed a transit of the candidate TOI-282.01 with *ASTEP* on the night of UT 2020 June 08 following our interest to confirm planets with long transits that we were particularly well able to observe during the austral winter. TOI-282.01 was identified by searching the TESS Transit Finder (Jensen 2013). Our detection of the full transit, the first of its kind as part of the photometric follow-up effort of TFOP (*TESS* Follow-up Observing Program) Sub-Group 1, prompted us to follow the system and look more closely at the available *TESS* data.

TOI-282.01 was observed on four further occasions by *ASTEP* (UT 2021 March 15, UT 2021 May 10, UT 2021 July 05, UT 2021 August 30) resulting in two partial transits and two non-detections due to poor weather.

TOI-282.03 was observed on the UT 2021 March 08 and again on the UT 2021 August 23. Both observations resulted in non-detections of the shallow event, but the field was cleared of NEBs within 2.5".

4.2.3 LCO

We observed TOI-282 in Pan-STARRS z-short band on UTC 2021 August 30 from the Las Cumbres Observatory Global Telescope (LCOGT; Brown et al. 2013) 1.0 m network node at Siding Spring Observatory. The 1 m telescopes are equipped with 4096×4096 SINISTRO cameras having an image scale of $0''389$ per pixel, resulting in a $26' \times 26'$ field of view. The images were calibrated by the standard LCOGT BANZAI pipeline (McCully et al. 2018), and photometric data were extracted using AstroImageJ (Collins et al. 2017). The target star was saturated to provide higher photometric precision for fainter stars nears within $2''5$ of the target star. The observations were scheduled to include ingress coverage for a transit of TOI-282.03 with more than $\pm3\sigma$ ephemeris coverage according to a public ephemeris from the SPOC pipeline. However, according to the linear ephemeris extracted in Section 5.1 of this work, the observations covered from the time of nominal ingress to 90 minutes later. According to the TTV analysis of Section 5.2, the ingress would have happened 45 minutes earlier than the linear ephemeris from this work on this epoch, resulting in all in-transit coverage. Although these data do not rule out nearby eclipsing binaries due to the ingress timing, we do not find an obvious deep event in any star within $2''5$ of the target star that could be the source of the TESS signal.

4.3 Radial Velocity Follow-up

We acquired 8 high-resolution spectra (R≈140 000) with the Echelle SPectrograph for Rocky Exoplanets and Stable Spectroscopic Observations (ESPRESSO; Pepe et al. 2021) on the 8.2 m ESO Very Large Telescope (VLT; Paranal observatory, Chile). The observations were performed in service mode between UT 2019 October 15 and UT 2019 December 27 as part of our program 0104.C-0003 (PI: Rodler). The exposure time was set to 1115 s, leading to a mean signal-to-noise (S/N) ratio of ~160 per pixel at 550 nm. We reduced the ESPRESSO data and extracted the radial velocity measurements

by employing ESO's ESPRESSO data reduction pipeline, version 2.2.1[5], reaching a mean RV precision of 1.1 m/s.

We also gathered 7 high-resolution spectra (R≈115 000) with the High Accuracy Radial Velocity Planet Searcher (HARPS; Mayor et al. 2003) spectrograph mounted at the 3.6 m ESO telescope (La Silla observatory, Chile), as part of ESO programs 60.A-9700 and 60.A-9707. The spectra were collected between UT 2019 May 24 and UT 2021 January 29, setting the exposure time to 1800 s, which led to a mean S/N ratio of ~100 per pixel at 550 nm. We reduced the spectra using the dedicated HARPS data reduction software (DRS) and extracted the radial velocity (RV) measurements by cross-correlating the Echelle spectra with a G2 numerical mask (Baranne et al. 1996; Pepe et al. 2002; Lovis & Pepe 2007). The resulting radial velocity measurements have a mean precision of 3.58 m/s

4.4 Validation

In this section we make use of data validation reports combined with our ground-based follow-up observations to validate the planetary nature of the three candidates orbiting TOI-282. The tests we describe here are standard procedure for the discovery of *TESS* planets, but we note again that for the two outer candidates the presence of anti-correlated TTVs render these steps somewhat redundant.

4.4.1 Vetting Tests

The *TESS* data validation report contains several tests to check the validity of the candidates (Twicken et al. 2018). These tests include checking for a difference in depth between odd and even transits, the presence of a potential secondary eclipse implying possible binarity, and any centroid offsets to ensure the event is on target. Both TOI-282.01 and .03 passed these tests successfully and were given false alarm probabilities of 2.14×10^{-162} and 2.21×10^{-34} respectively, indicating that these events are highly unlikely to be instrumental in nature. Having passed these tests, these candidates were ripe for follow-up observations to validate their planetary nature.

The false alarm probability for TOI-282.04 was calculated by Sherlock as 8×10^{-5}; Sherlock also provides a vetting stage for promising signals, where Field Of View (FOV) plots are generated through the internal usage of TPFPlotter (Figure 5) (Aller et al. 2020) to check for possible contamination sources; it also injects the search results into Latte (Eisner et al. 2020), which is used as the main vetting engine. Sherlock also provides folded lightcurves to check for even/odd transits and discard the detection of harmonics or sub-harmonics of the real signal. We scrutinise the data validation report produced by Latte and note no centroid offsets at the time of transits, nor were there any sharp changes in background flux.

4.4.2 Ruling Out False Positives

Nearby eclipsing binaries (NEB) scenarios were ruled out for all three candidates by the photometric observations, as described in Section 4.2.1. Subsequent observations of TOI-282.01 by *ASTEP* later further confirmed the events on target with clear detections of the transits.

Additionally, our high-resolution observations described in Section 4.1 rule out any blended bound companions down to a projected orbital separation of 2.8AU. A 0.1 $M_\odot$ companion at this orbital

---

[5] https://www.eso.org/sci/software/pipelines/espresso/espresso-pipe-recipes.html

separation would produce an RV variation of ~ 1.6 km/s. The very low scatter in our radial velocity measurements described in Section 4.3 rules out the presence of any bound stellar-mass companions in the system.

4.4.3 Statistical Validation with SHERLOCK and TRICERATPOS

SHERLOCK uses the statistical validation package TRICERATPOS presented in Giacalone et al. (2021) to calculate the false positive probability (FPP) for each of the candidates. TRICERATPOS queries the *TESS* Input Catalog (TIC) for stars within 10 pixels of the target and calculates the probability that the transits detected are caused by false positive scenarios. In all, 18 scenarios are tested, including that the signal is caused by a transiting planet on the target star with the input orbital period. SHERLOCK automates the preparation stage for TRICERATOPS by preparing the lightcurves and apertures; the statistical validation is then carried out five times to produce mean probabilities for each scenario.

The criteria for statistical validation of a planetary candidate is stated as FPP < 0.015; we compute FPPs of 0.0075, 0.035 and 0.203 for TOI-282.01, .03 and .04 respectively. This immediately places TOI-282.01 well below the threshold for validation, although the probability remains too high for TOI-282.03 and .04.

However, we are able to add further to this body of evidence by returning to the fact that this is a multi-planet system. Lissauer et al. (2012) derived an expression for a 'multiplicity boost', where the presence of additional planets in the same aperture increases the probability that the signals are planetary in nature:

$$P_3 \approx \frac{50 P_1}{50 P_1 + (1 - P_1)} \quad (1)$$

Where P_1 is the probability of planethood without taking the additional planets into account, and P_3 if the probability with the 3-planet multiplicity boost. This decreased the FPP for TOI-282.01, .03 and .04 to 0.00015, 0.0007 and 0.005 respectively. All three planets now meet the criteria for statistical validation showing that overwhelmingly, the planet hypothesis is the most favoured. We note that while the multiplicity boost described about was developed for *Kepler* candidates, a similar boost for *TESS* candidates is described in Guerrero et al. (2021) which for small planets (R < 6$R_\oplus$) decreases the FPP by a factor of ≈ 54. We choose to apply the boost described in Lissauer et al. (2012) as it is more conservative.

4.5 Validation Conclusions

Having ruled out all astrophysical false positive scenarios, calculated false positive probabilities and taken into account multiplicity we can now consider the system validated.

From this point on we refer to the three validated planets by their formal names in order of increasing semi-major axis:

- TOI-282.04 → HD 28109 b
- TOI-282.01 → HD 28109 c
- TOI-282.03 → HD 28109 d

5 ANALYSIS

With the planetary nature of the signals validated, we now present our analysis of all available data for HD 28109 b, c and d. We begin by describing our global analysis of the available photometry for the system in Section 5.1, followed by our dynamical analysis in Section

5.2. In Section 5.3 we make use of priors from our photometric and dynamical fits to fit the available radial velocity data.

5.1 Global Photometric Analysis

We carried out a global photometric analysis of the datasets described in Section 4 using ALLESFITTER (Günther & Daylan 2021, 2019). ALLESFITTER is a publicly available versatile inference package capable of jointly fitting photometric and radial velocity datasets from different instruments using ELLC (Maxted 2016) for lightcurve and RV models, EMCEE (Foreman-Mackey et al. 2013) for MCMC, DYNESTY (Speagle 2020) for dynamic nested sampling, and CELERITE (Foreman-Mackey et al. 2017) for Gaussian Process (GP) models. We chose to use this package as it can simultaneously fit for white (uncorrelated) noise and red (correlated) noise for different instruments, while offering a wide selection of models to choose from and compare evidence.

We adopted the signal parameters found in Section 3.3 as uniform priors, and the stellar parameters derived in Section 2 as Gaussian priors and we fit using the nested sampling algorithm. Nested sampling (Skilling 2004) works by drawing a number of live points from the prior distribution, and then removing the point with the lowest likelihood. Another point is then drawn from the prior while requiring that the overall likelihood now be higher than before. This process then repeats until the change in Bayesian evidence, parametrised as $\Delta \ln Z$, falls below a certain threshold. We begin the algorithm with 1500 live points and set the threshold to $\Delta \ln Z < 0.01$ as recommended by the ALLESFITTER documentation.

We computed quadratic limb darkening coefficients u_1 and u_2 for HD 28109 in *TESS* and R_c filters using PYLDTK (Parviainen & Aigrain 2015) and the PHOENIX stellar atmosphere library provided by (Husser et al. 2013). The resulting coefficients are presented in Table 3; these are also input to our global fit as Gaussian priors.

We initially fit for a two-planet model using only HD 28109 c and HD 28109 d, and then for a three-planet model incorporating HD 28109 b. One of the key advantages of nested sampling over MCMC (Markov Chain Monte Carlo) is the calculation of the Bayesian evidence at each stage of the algorithm; this allows us to determine which model is statistically favoured by calculating the Bayes' factor (Kass & Raftery 1995). In both cases, we fit simultaneously for all transit parameters, quadratic stellar limb-darkening coefficients in the Kipping (2013) parametrisation, as well as the baseline model and the white noise scaling for each instrument. These latter two ensure that uncertainties arising from instrument systematics are appropriately propagated to derived physical parameters.

In Section 3.3 we found that all three planets had the highest SNR in *TESS* when the flux was detrended; to detrend the data for semi-periodic stellar variability (red noise) present in all instruments, we simultaneously fit a GP using a Simple Harmonic Oscillating (SHO) kernel. The parametrisation used in the fit is summarised in Table 3.

We find that the 3-planet model is vastly statistically favoured over the 2-planet model, with a Bayes Factor in excess of 60 000. A $BF > 150$ is usually considered strong enough statistical evidence to confirm a more complex model (Kass & Raftery 1995). The fit's result further confirms the existence of HD 28109 b in our data.

In both the 2- and 3-planet model fits, eccentricity and argument of periastron were set as free parameters. We note that the resulting derived orbital parameters suggest that the two outer planets could have small to moderate eccentricities ($e_c = 0.116^{+0.30}_{-0.079}$ and $e_d = 0.19^{+0.34}_{-0.15}$) and yield calculated host densities within 1σ of the prior, while the inner planet yields a very large eccentricity of
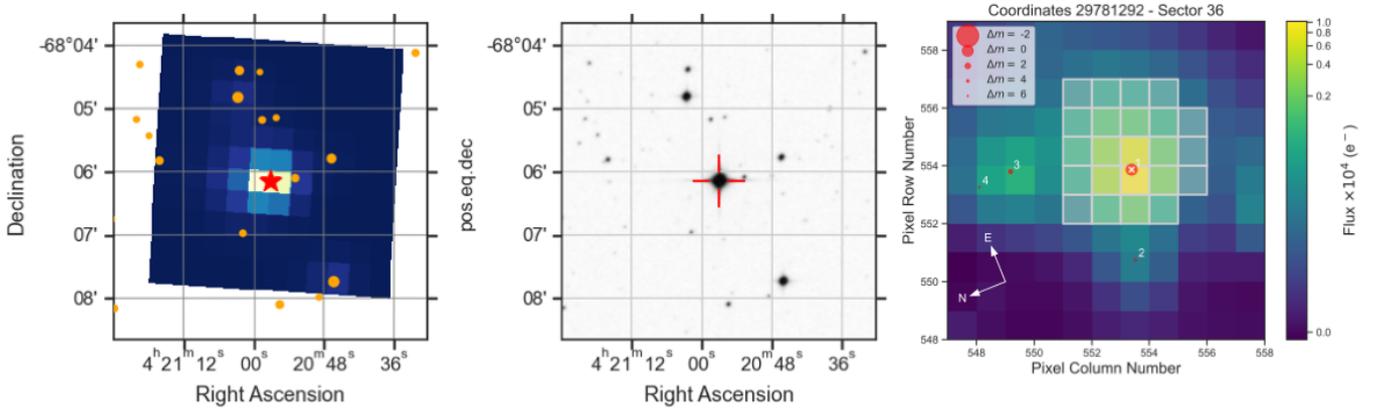
Figure 5. Images of the field of TOI-282/HD 28109, showing that the star does not have any bright contaminating sources nearby. **Left Panel:** Target pixel files showing TOI-282 as a red star and other nearby sources as orange circles. The size of the circles is representative of the source's brightness. **Middle Panel:** Sloan Digital Sky Survey (SDSS York et al. 2000) image of the surrounding field of TOI-282 (indicated by a red cross). **Right Panel:** *TESS* target pixel file of one of the 25 sectors in which TOI-282 was observed, created with TPFPLOTTER (Aller et al. 2020). The pipeline aperture is shown by the white shaded region, and all nearby sources from Gaia (Gaia Collaboration et al. 2018) down to a magnitude difference $\Delta M = 8$ are overplotted as red circles.

$e_b = 0.809^{+0.049}_{-0.083}$ and a calculated host density 5-σ below the prior. The host density is calculated from the transit parameters of each planet individually by ALLESFITTER using the expression presented in Seager & Mallén-Ornelas (2003):

$$\rho_{\star,\mathrm{obs}} \equiv \frac{3\pi (a/R_\star)^3_{obs}}{GP^2} \qquad (2)$$

where $\rho_{\star,\mathrm{obs}}$ is the host density derived from transit parameters assuming a Keplerian circular orbit. The manner and extent of the discrepancy between $\rho_{\star,obs}$ and the external prior on stellar density can be indicative of erroneous assumptions made regarding the orbits (Kipping 2014). In particular, for such an eccentric orbit we would expect the ratio ρ_{obs}/ρ_{true} to be much greater than unity.

We therefore repeat the 2- and 3-planet fits constraining eccentricities to zero and then compare the evidence for each of the models to see which is statistically most likely. We find that all 3-planet models are preferred over all 2-planet models, with Bayes Factors in excess of 50 000. We also find that all circular models are preferred over models with non-zero eccentricities. In the case of the 3-planet circular model vs. the 3-planet eccentric model we find a Bayes Factor of almost 3 000, indicating that a more complex lightcurve modelling with eccentric orbits is not preferred.

The results of the global fit, including derived parameters, are presented in Table 3. In Figure 6 we present the three individual *ASTEP* transits for planet c along with the best fitting model, and in Figure 7 we present the *TESS* phase folded lightcurves for each planet along with the best fitting model.

5.2 Dynamical Analysis

In this section we consider a non-Keplerian model for the planets of HD 28109; we first fit individual transit times and then use these timings to infer dynamical masses for the planets.

5.2.1 Transit Timing Variations

Given the proximity of the two outer planets to a first order 3:2 mean-motion resonance (within ∼ 0.3%), we would expect these planets to experience some mutual gravitational influence leading to transit timing variations (TTVs). This is supported by visual inspection
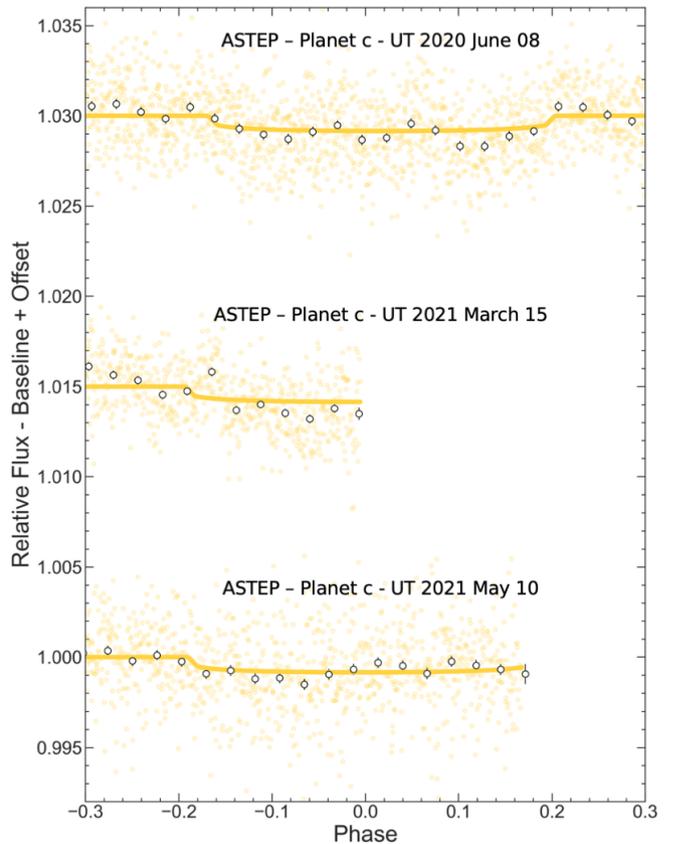

Figure 6. Detrended transits observed with *ASTEP* on the nights of 2020 June 08, 2021 March 15 and 2021 May 10. The green points are the detrended flux, while the white circles are binned. Curves superimposed are the best-fitting models for each transit.

of the individual transit fits resulting from the nested sampling, as several appear to have noticeable offsets in time between the model and the data.

We therefore re-fit the photometry once again using ALLESFITTER, this time allowing the midtime of each individual transit to vary about a linear ephemeris for all three planets.

Table 3. Priors used in our fit, along with fitted and derived parameters. Uniform priors are indicated as $\mathcal{U}$(lower bound, upper bound) and normal priors are indicated as $\mathcal{N}$(mean, standard deviation).

	HD 28109 b	HD 28109 c	HD 28109 d	Source
Fit Parametrisation and Priors				
Transit Depth $R_p/R_\star$	$\mathcal{U}(0.008, 0.015)$	$\mathcal{U}(0.023, 0.035)$	$\mathcal{U}(0.017, 0.037)$	
Inverse Scaled Semi-major Axis $(R_\star + R_p)/a$	$\mathcal{U}(0.05, 0.06)$	$\mathcal{U}(0.015, 0.035)$	$\mathcal{U}(0.015, 0.03)$	
Orbital Inclination $\cos i$	$\mathcal{U}(0.000, 0.04)$	$\mathcal{U}(0.000, 0.04)$	$\mathcal{U}(0.000, 0.04)$	
Transit Epoch T_0	$\mathcal{U}(2458344.7, 2458344.9)$	$\mathcal{U}(2458337.12, 2458337.32)$	$\mathcal{U}(2458355.58, 2458355.98)$	
Planet Mass $M_p/M_\star$	$\mathcal{U}(0.0, 0.000026)$	$\mathcal{U}(0.0, 0.0005)$	$\mathcal{U}(0.0, 0.0005)$	
Period P	$\mathcal{U}(22.8, 23.0)$	$\mathcal{U}(55.6, 56.6)$	$\mathcal{U}(84.2, 86.0)$	
Eccentricity e	$\mathcal{U}(0.0, 0.5)$	$\mathcal{U}(0.0, 0.5)$	$\mathcal{U}(0.0, 0.5)$	
Longitude of Periapsis ϖ	$\mathcal{U}(0, 360)$	$\mathcal{U}(0, 360)$	$\mathcal{U}(0, 360)$	
Limb Darkening Coefficients				
TESS u_1	0.4041 ± 0.0007	ASTEP u_1	0.4758 ± 0.0009	
TESS u_2	0.1324 ± 0.0018	ASTEP u_2	0.1392 ± 0.0022	
TESS q_1	$\mathcal{N}(0.2878, 0.0024)$	ASTEP q_1	$\mathcal{N}(0.3782, 0.0034)$	
TESS q_2	$\mathcal{N}(0.3766, 0.0013)$	ASTEP q_2	$\mathcal{N}(0.3868, 0.0014)$	
External Priors		**GP Priors**		
Stellar Mass $M_\star$	$\mathcal{N}(1.26, 0.08)$	Amplitude Scale gp $\ln S_0$ (flux)	$\mathcal{U}(-15, 5)$	
Stellar Radius $R_\star$	$\mathcal{N}(1.446, 0.035)$	Damping gp $\ln Q$ (flux)	$\mathcal{U}(-10, 10)$	
Stellar Effective Temperature T_{eff}	$\mathcal{N}(6120, 50)$	Frequency gp $\ln \omega_0$ (flux)	$\mathcal{U}(-10, 10)$	
Fitted Parameters				
$R_p/R_\star$	$0.01441^{+0.00031}_{-0.00037}$	0.02632 ± 0.00027	$0.01999^{+0.00035}_{-0.00037}$	Fixed Lin. Ephem. Fit
$(R_\star + R_p)/a$	$0.05017^{+0.00022}_{-0.00012}$	$0.02231^{+0.00073}_{-0.00066}$	$0.01688^{+0.00053}_{-0.00047}$	Fixed Lin. Ephem. Fit
$\cos i$	$0.03964^{+0.00024}_{-0.00040}$	$0.0081^{+0.0018}_{-0.0021}$	$0.0064^{+0.0013}_{-0.0015}$	Fixed Lin. Ephem. Fit
T_0 (BJD)	$2458344.81772 \pm 0.00757$	$2458377.80109^{+0.00724}_{-0.00733}$	$2458355.67324 \pm 0.00432$	Dynamical Fit
P (d)	$22.89104^{+0.00035}_{-0.00036}$	$56.00819^{+0.00194}_{-0.00202}$	$84.25999^{+0.00744}_{-0.00662}$	Dynamical Fit
e	< 0.3307	< 0.1203	< 0.0864	Dynamical Fit
Fitted RV Jitter		**Fitted GP Hyperparameters**		
$\ln \sigma_{jitter;HARPS}$ ($\ln$ km/s)	$-7.8^{+1.6}_{-2.8}$	gp $\ln S_0$ (flux)	$-19.72^{+0.20}_{-0.19}$	Fixed Lin. Ephem. Fit
$\ln \sigma_{jitter;espresso}$ ($\ln$ km/s)	$-5.99^{+0.38}_{-0.36}$	gp $\ln Q$ (flux)	$-4.9^{+1.9}_{-2.2}$	Fixed Lin. Ephem. Fit
		gp $\ln \omega_0$ (flux)	$6.0^{+2.2}_{-1.9}$	Fixed Lin. Ephem. Fit
Derived Parameters				
Companion radius; R_p ($R_\oplus$)	$2.199^{+0.098}_{-0.10}$	4.23 ± 0.11	3.25 ± 0.11	Fixed Lin. Ephem. Fit
Semi-major axis; a (AU)	0.1357 ± 0.0034	0.308 ± 0.011	0.411 ± 0.016	Fixed Lin. Ephem. Fit
Inclination; i (deg)	$87.725^{+0.023}_{-0.012}$	$89.543^{+0.093}_{-0.086}$	$89.682^{+0.093}_{-0.082}$	Fixed Lin. Ephem. Fit
Impact parameter; b	$0.8007^{+0.0055}_{-0.0084}$	$0.365^{+0.058}_{-0.068}$	$0.339^{+0.075}_{-0.093}$	Fixed Lin. Ephem. Fit
Total transit duration; T_{tot} (h)	$5.392^{+0.10}_{-0.073}$	8.973 ± 0.060	$10.13^{+0.14}_{-0.11}$	Fixed Lin. Ephem. Fit
Full-transit duration; T_{full} (h)	$4.997^{+0.11}_{-0.081}$	8.425 ± 0.070	$9.66^{+0.14}_{-0.12}$	Fixed Lin. Ephem. Fit
Equilibrium temperature; T_{eq} (K)	881.2 ± 7.5	$585.2^{+8.7}_{-8.3}$	$506.5^{+8.7}_{-8.0}$	Fixed Lin. Ephem. Fit
Transit depth TESS; $\delta_{tr;TESS}$ (ppt)	$0.188^{+0.013}_{-0.016}$	$0.834^{+0.015}_{-0.017}$	$0.489^{+0.021}_{-0.024}$	Fixed Lin. Ephem. Fit
Transit depth ASTEP; $\delta_{tr;ASTEP}$ (ppt)	-	$0.854^{+0.016}_{-0.018}$	-	Fixed Lin. Ephem. Fit
Companion TTV mass; $M_{p;TTV}$ ($M_\oplus$)	-	$7.943^{+4.227}_{-3.046}$	$5.681^{+2.738}_{-2.110}$	Dynamical Fit
Companion RV mass; $M_{p;RV}$ ($M_\oplus$)	$18.496^{+9.120}_{-7.609}$	-	-	RV Fit

When allowing for TTVs, we fit for all the same parameters as in the linear fit, except that we now fix the linear ephemeris using the values derived from the most statistically favoured fit in Section 5.1. We also constrain eccentricities to zero for all three planets and once again apply Gaussian priors on the stellar density and quadratic limb darkening coefficients.

In preparation for a TTV fit, Allesfitter attempts to guess the location of the flux minimum during each transit present in the data, with these guesses then used as uniform priors for the fit. However, we find that almost all of the guesses for planet b are affected by local stellar variability or nearby transits of other planets biasing the fit; instead, for each transit's mid-time, we impose a uniform prior defined as the linear predictions ± 120 minutes for all planets. Once again we simultaneously fit a GP with a SHO kernel to account for stellar variability.

The results of this fit are presented in Figure 8. HD 28109 c and d present very clear and significant anti-correlated TTVs with peak to peak amplitudes of ~ 50 mins and ~ 100 mins respectively. While the shifts in timing do appear to show a sinusoidal variation between early and late, it is most likely that what we see here is the shorter term 'chopping' part of the signal (Deck & Agol 2015) given that the 'Super-Period' for these planets is expected to be in excess of 9 000 days.

For HD 28109 b the errors on the timings are very large due to how shallow individual events are (≈ 0.19ppt) and therefore our results are consistent with no TTVs. We note that for some individual events the errors were significantly smaller than average. Visual inspection of each transit fit showed that this is probably caused by artifacts in the lightcurves. We therefore amplified the errors on all timings of planet b to be at least the mean timing uncertainty.
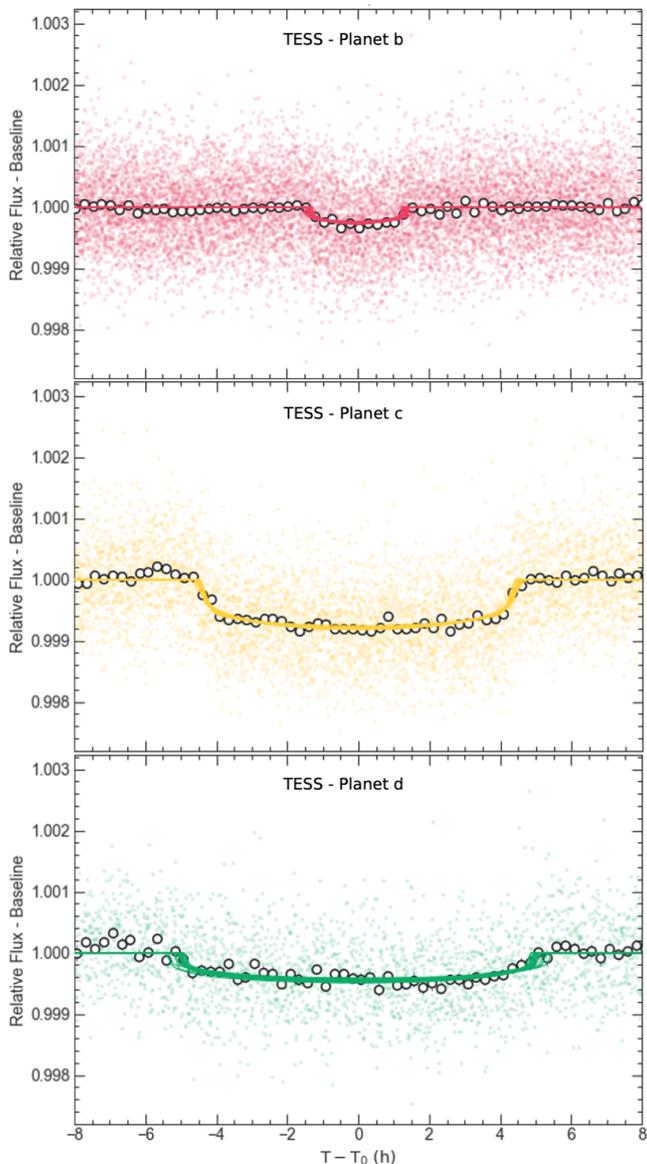
Figure 7. Global fit of the *TESS* photometric data for each of the planets of HD 28109. Points in the background are the phase-folded 2-minute cadence data, while white circles are the binned points. Curves are 20 samples drawn from the posterior.
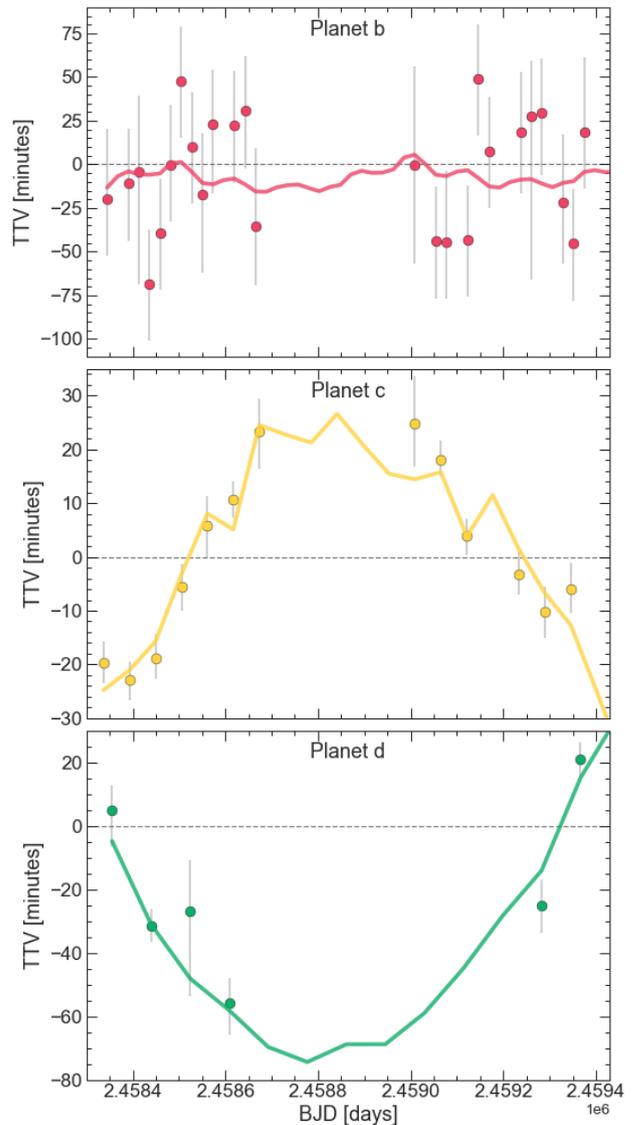

Figure 8. Transit timing variations (in minutes) for each of the planets of HD 28109 spanning two years of *TESS* data plus ground-based photometric monitoring of planet c. The points show the difference between the fitted mid-times and the linear predictions, while the lines show the model predictions from our dynamical analysis in Section 5.2.2.

5.2.2 *Mass Estimates From TTVs*

We perform dynamical analysis of the observed transit times with a symplectic *N*-body integrator code described in Nesvorný et al. (2012). We instruct the code to simultaneously fit all measured transit times, using MULTINEST (Feroz & Hobson 2008) to perform the regression, setting the integration time-step to 0.5 d, roughly 1/50 of the planet b's orbital period. We consider dynamical models with 2, 3 and 4 planets. The model with 3 planets has 20 parameters: planet-to-star mass ratios, orbital periods, eccentricities, longitudes of periapsis, impact parameters, difference in nodal longitudes, and reference epochs between a reference time (2458337 BJD UTC) and the first observed transit of each planet. The nodal longitude of the innermost planet in each fit is fixed at 270°, and therefore the 2 and 4 planet models have 13 and 27 parameters, respectively. We use uniform priors for all parameters except for the impact parameter, since our light-curve fits provide strong constraints which are used here.

The host star mass was fixed at $M_\star = 1.26\ M_\odot$. The uncertainties discussed below therefore do not account for the uncertainty in the stellar mass.

We find that the existing measurements are not good enough to uniquely determine the planet properties. The first problem arises because there is a large radial separation between the inner planet b and the two outer planets: the measured TTVs of c and d thus most likely reflect their mutual interaction (rather than those of planet b). In addition, given the relatively large measurement errors of b's TTVs it is not clear whether b's TTVs contain any useful information about planets c and d. Thus, as b can be decoupled from the rest of the system it is difficult to meaningfully constrain its properties. Indeed, when we instruct MULTINEST to perform a 3-planet fit, the mass of planet b always reaches to the upper edge of the mass prior even if this is clearly nonphysical (i.e., mass exceeding that of Jupiter for
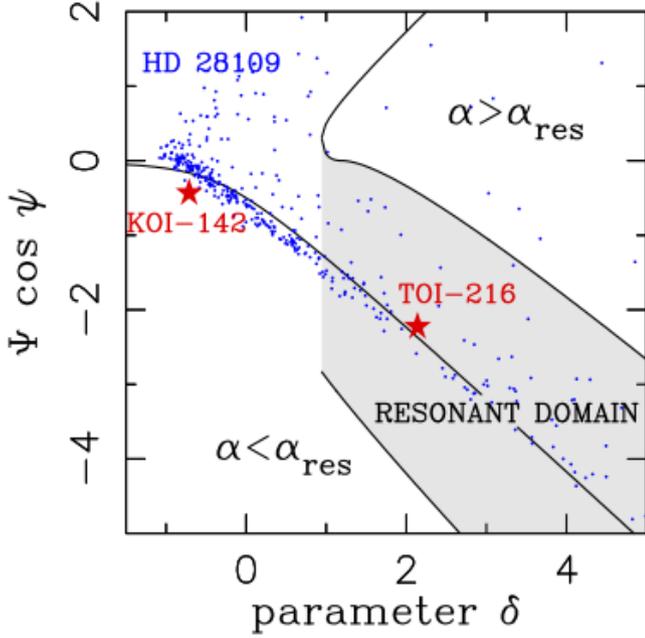
Figure 9. The 3:2 resonance structure diagram following Nesvorný & Vokrouhlický (2016). Systems with $\alpha = a_c/a_d < \alpha_{res}$ ($\alpha > \alpha_{res}$), where $\alpha = 0.763$ corresponds to the exact resonance, have orbits just wide (narrow) of the resonance. The resonance region where ψ librates is shaded. The separatrices and stable point are solid. Three planetary systems are plotted: HD 28109 (this work), TOI-216 (Dawson et al. 2021; Nesvorny et al. 2021) and KOI-142 (Nesvorný et al. 2013). TOI-216 is firmly in the resonance and KOI-142 is firmly outside the resonance. For HD 28109, the blue dots show a sample of 500 posterior solutions from our dynamical 3-planet fit, of which roughly two-thirds are non-resonant and roughly one-third are resonant.

Figure 10. Model predictions of the transit timings variations for the planets of HD 28109 for the next 11 000 days, spanning more than one full TTV period for the two outer planets.

the estimated radius $R_b = 2.199\ R_\oplus$). We therefore limit the uniform prior on the mass of planet b to $M_b = 11 M_\oplus$.

All fits performed here confirm that the masses of c and d are in the planetary range. Our best fit indicates $m_c/M_* = (1.9^{+1.0}_{-0.7}) \times 10^{-5}$ and $m_d/M_* = (1.4^{+0.6}_{-0.5}) \times 10^{-5}$, suggesting that both planets have low densities. The orbital eccentricities of c and d are most likely low ($e < 0.1$), but some 2-planet fits identify modes with eccentric orbits ($e > 0.1$). In Table 3 we present the 2σ upper limits for the eccentricities of all three planets as this parameter remains poorly constrained; the mean values of the posterior distributions for the eccentricities are $e_b = 0.1519^{+0.0894}_{-0.0944}$, $e_c = 0.0391^{+0.0406}_{-0.0231}$, and $e_d = 0.0238^{+0.0313}_{-0.0157}$. The posteriors for the longitude of periastron are not included in Table 3 as they are unconstrained by our fits.

Given the wide orbital separation between planets b and c, we perform an additional fit including a putative fourth planet. This planet may be non-transiting or too small to be detected. We used a uniform prior between 28 d to 44 d for the 4th planet orbital period. The 4-planet fits give masses of c and d that are consistent with the masses reported above (and low orbital eccentricities). The best parameters for the hypothetical 4th planet are $m_4/M_* \simeq 7.6 \times 10^{-6}$ and $P_4 \simeq 39.3$ d. With this orbit, the two inner planets would be wide of the 3:2 resonance. The Bayesian evidence for this fit is significantly lower than for the 3-planet fit, indicating that the 3-planet fit is preferred.

The eccentricities of planets c and d are low and when that is the case, the resonant and near-resonant dynamics can be studied analytically following Nesvorný & Vokrouhlický (2016). There are three variables to consider, each of them being a combination of orbital
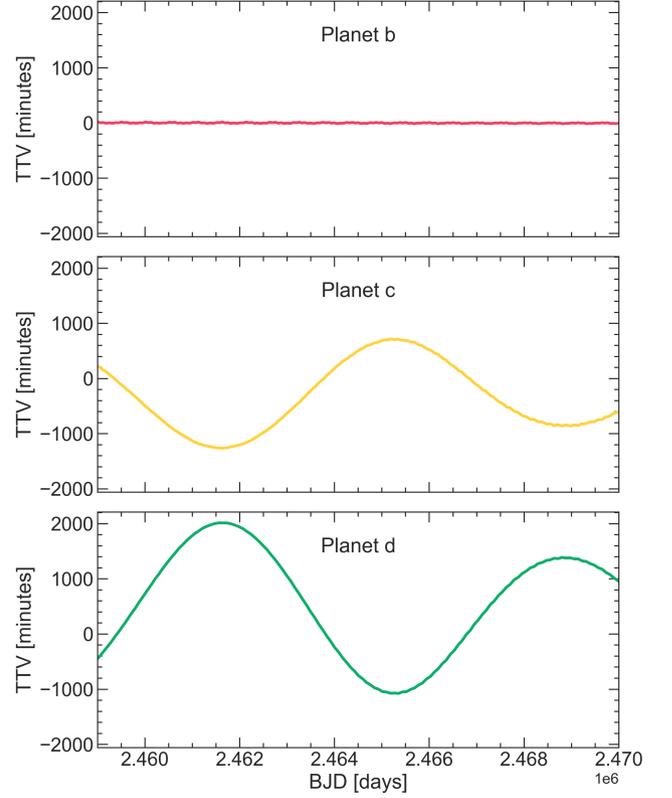
elements. Constant δ is an orbital invariant that defines the position of the system relative to the 3:2 resonance, the resonant angle ψ is a function of the usual 3:2 resonant angles σ_1 and σ_2, and variable Ψ is a combination of planetary masses, semi-major axes and eccentricities (see Nesvorný & Vokrouhlický (2016) for details). The resonant librations of ψ can only happen for $\delta > 0.945$. Figure 9 shows position of planets c and d in the terms of the dynamical variables δ, ψ, and Ψ. About two thirds of the posterior samples are non-resonant with the two orbits being slightly wide of the exact resonance. About one third of the sample, however, show resonant librations with a generally low libration amplitude. Additional observations will be needed to better constrain the location of the c and d planets relative to the 3:2 resonance.

We predict that the amplitudes of the TTVs will be very large (~ 1000 min for planet c and ~ 2000 min for planet d) once one whole TTV period has been sampled. In Figure 10 we present the predicted TTVs of the system for the next 11 000 days. Continued monitoring of the system will allow us to both improve timing predictions and refine the dynamical mass measurements of planets c and d.

5.3 Radial Velocity Analysis

The global photometric analysis yielded strong priors on all orbital parameters; additionally, we can place priors on the masses of the two outer planets from the dynamical fit. We therefore fit the radial velocity data set to gain an estimate on the mass of the innermost planet using ALLESFITTER. We adopt Gaussian priors on the all orbital parameters for the three planets (P, T_0, , R_p/R_*, $(R_*+R_p)/a$, cos$i$,), as well as the radial velocity semi-amplitudes of the outer planets (K).

We place a wide uniform prior between $0.1 - 6.0$ m/s (corresponding to $0.5 - 30$ M$_\oplus$) on the semi-amplitude of the inner planet and fit for all three periods, reference times and semi-amplitudes. In our models, we vary the RV offset and RV jitter for each individual dataset. The jitter parameter appears as an additional RV noise term added in quadrature to the nominal RV uncertainties and subsums any instrumental or stellar effects (such as activity) not considered by the formal RV errors.

In Figure 11 we present the phased radial velocity curves. The radial velocity semi-amplitude posterior for the inner planet yields a mass estimate of M$_b$ = $18.50^{+9.12}_{-7.61}$ M$_\oplus$; for the outer planets we find mass estimates consistent with the estimates from the dynamical analysis: M$_c$ = $7.99^{+2.13}_{-2.03}$ M$_\oplus$ and M$_d$ = $5.53^{+0.98}_{-0.94}$ M$_\oplus$. We do however note that to precisely constrain the masses of the system far more measurements are needed, and therefore this result is just a first estimate.

6 SYSTEM DISCUSSION

HD 28109 is host to at least three planets, with two very close to a first order mean-motion resonance. So far, this is the brightest *TESS* star, and the third brightest star overall, known to host TTV planets. In Figure 12 we present the current sample of planets known to show transit timing variations in multi-planetary systems, plotted as planet radius and orbital period vs. host V magnitude, highlighting the position of the three planets of the HD 28109 system[6]. Planets plotted as dark grey circles have measured masses (by RV or TTV) while grey circles have masses estimated by mass-radius relations. The only host brighter than HD 28109 known to host TTV planets with measured masses is WASP-18, but as the outer planet is non-transiting full characterisation of the system is not yet possible (Pearson 2019).

In this section we discuss the system in the context of other known exoplanetary systems, and current and near-future instrumentation capabilities.

6.1 The planets of HD 28109 on the Mass-Radius Diagram

In Figure 13 we present a Mass-Radius diagram showing the positions of HD 28109 b, c, and d in relation to other known exoplanets with masses measured using TTVs or precise radial velocities. The mean densities of Earth, Neptune, Saturn and pure iron are also shown.

The masses of HD 28109 c and d estimated from TTVs indicate that they are under-dense compared with most other sub-Neptunian mass planets. Given the paucity of planets in this size and mass regime with precisely constrained parameters at orbital separations comparable to HD 28109 b and c, we cannot determine at this time whether or not their densities are truly anomalous.

The mass estimate of HD 28109 b is rather more puzzling. First estimates from radial velocities in this work suggest that this planet is significantly denser than typical planets of its size. Atmospheric escape in sub-Neptunes is thought to be driven by photoevaporation (Owen & Wu 2013) and/or core-powered mass loss (Ginzburg et al. 2018). At its orbital separation, the gravity of planet b would be sufficient to retain a H/He dominated envelope if stellar irradiation is the main driver (Jin & Mordasini 2018). Should the large mass be

---

[6] Data for this plot was retrieved from the NASA Exoplanet Archive (Akeson et al. 2013) on 2021 October 20: https://exoplanetarchive.ipac.caltech.edu/cgi-bin/TblView/nph-tblView?app=ExoTbls&config=PSCompPars.
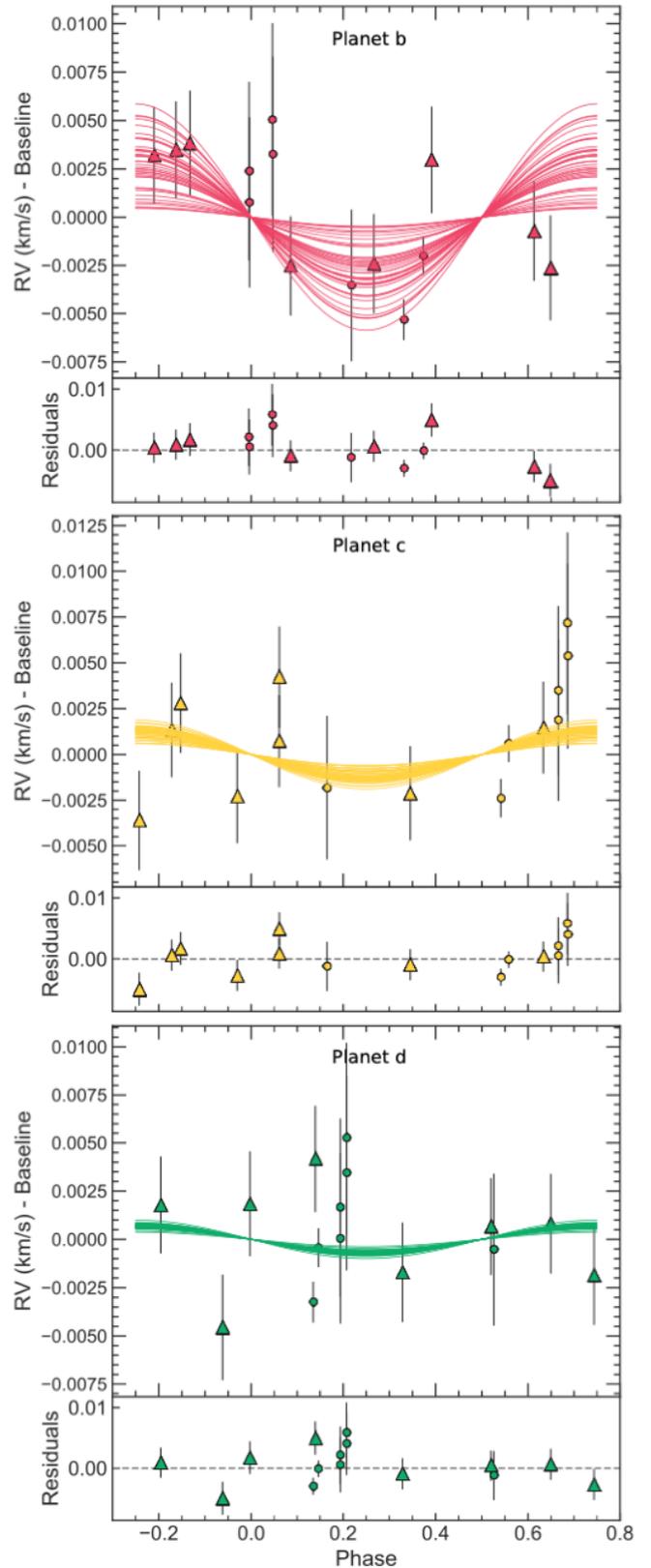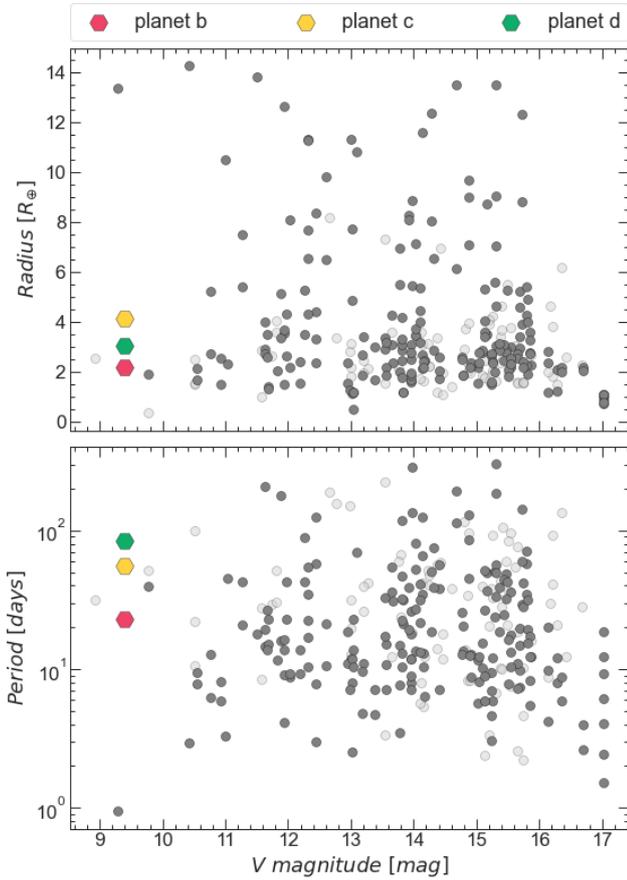
Figure 11. Phased radial velocity measurements for each of the three planets. Triangles are points from ESPRESSO, while circles are points from HARPS; the curves are 20 model samples from the posterior. The data uncertainties include the RV jitter.

Figure 12. Distribution of known multi-planetary systems exhibiting transit timing variations. The planets of HD 28109 are shown as hexagons in violet (planet b), green (planet c) and pink (planet d); other planets are either shown in dark grey if the have a measured mass (by RV or TTV) or light grey if they do not. In the upper panel we show the distribution in planet radius according to host star *V* mag, while in the bottom panel we show the distribution in orbital period.

confirmed with radial velocities, it could favour core-powered mass loss as the main driver atmospheric escape in this scenario, as the heat source is the planet's own residual formation energy (Gupta & Schlichting 2020).

Given the two outer planets' relatively large orbital radii (> 50 days), it is unlikely that they suffered major mass loss (Gupta & Schlichting 2020). Preliminary models of the contraction of the planetary envelope based on the approach used by Guillot et al. (2006) and Valencia et al. (2010) and neglecting the core luminosity indicate that matching their mass, radius and age require a hydrogen-helium envelope which consists of 19% of the planetary radius for planet c and 10% for planet d. Such a relatively significant envelope mass fraction may result from a formation at large orbital distances (Lee & Chiang 2016). These values are to be considered with caution however because including core luminosity and tidal heating that may be caused by the resonances would yield smaller envelopes (Millholland 2019).

Planets with vastly different densities within the same system, which is likely to be the case for TOI-282, provide invaluable laboratories to explore the various outcomes of planet formation with the same conditions.

6.2 Prospects For Precise Mass Measurements With Radial Velocities

Stellar activity in HD 28109 poses a challenge on RV follow-up observations given the small RV semi-amplitudes of these planets. In our RV analysis, we find that the RV jitter terms in the HARPS and ESPRESSO measurements are on the order of 2.4 m/s and 0.4 m/s , respectively (Table 3). Given the TTV masses of planets c and d, their expected RV semi-amplitudes are $K_c \approx 1.14$ m/s and $K_d \approx 0.71$ m/s. For planet b, the range is broad, spanning from the Chen & Kipping (2017) estimate to the mass of a pure iron planet, $K \approx 0.91 - 2.4$ m/s. Given the length of the period of the outermost planet, sampling the full orbit will be a considerable undertaking.

With the goal to further characterize the system, we are currently conducting a radial velocity survey with ESPRESSO; once concluded, the results will be presented in a follow-up paper. These high-precision radial velocity measurements will help to disentangle the eccentricity of planet b, as well as shed light on the possible presence of additional non-transiting planets in the system. In addition, these measurements will finally put precise constraints on the masses of these planets, which will be crucial for atmospheric follow-up observations.

6.3 Dynamical Exploration of Planet b's Parameters

Our dynamical and photometric fits provided us with TTV mass estimates for the two outermost planets, along with strong evidence for circular orbits. However, the mass and eccentricity of planet b remain largely unconstrained, and a dynamical analysis might be able to restrict plausible parameters of planet b. The first 3-planet photometric fit in Section 5.1 found an eccentricity of ~0.8, while the dynamical fits presented in Section 5.2.2 favour an eccentricity of ~0.17.

We use the Mean Exponential Growth factor of Nearby Orbits chaos index ($Y(t)$, MEGNO; Cincotta & Simó 2000) to assess the stability of the HD 28109 system with the full range of eccentricity and mass estimates for planet b. MEGNO is used to evaluate whether a body's trajectory will be stable following perturbations of its initial conditions. The time-averaged MEGNO $\langle Y(t) \rangle$ will tend to 2 for $t \rightarrow \infty$ if the motion of the body is quasi-periodic, while chaotic behaviour will cause $\langle Y(t) \rangle$ to tend to infinity instead.

We made a 50×50 mass-eccentricity grid for planet b with eccentricity values evenly spaced between $0 - 0.8$, and masses evenly spaced between $5 - 30 \, M_\oplus$. We used the MEGNO implementation of the N-body integrator REBOUND (Rein & Liu 2012) which in turn uses the Wisdom-Holman WHFAST code (Rein & Tamayo 2015). We used steps of 1/50th of the period of planet b (0.5 days) and integrated for 10 000 orbits of the outermost planet (~ 2 300 years) to construct a two-dimensional MEGNO map. We find that the full mass range is non-chaotic but only for eccentricities smaller than ~0.4; eccentricities up to ~0.5 can be stable but only for the largest masses in the range we tested. This indicates that a wide range of mass values are possible for planet b, in line with the wide mass prior used for our dynamical and RV fits.

6.4 Prospects For Atmospheric Characterisation with *HST* and *JWST*

To assess the suitability of HD 28109 b, c and d for atmospheric characterisation using transmission and emission spectroscopy, we calculated for each planet the Transmission and Emission Spectroscopy Metrics following Kempton et al. (2018). The TSMs for each planet
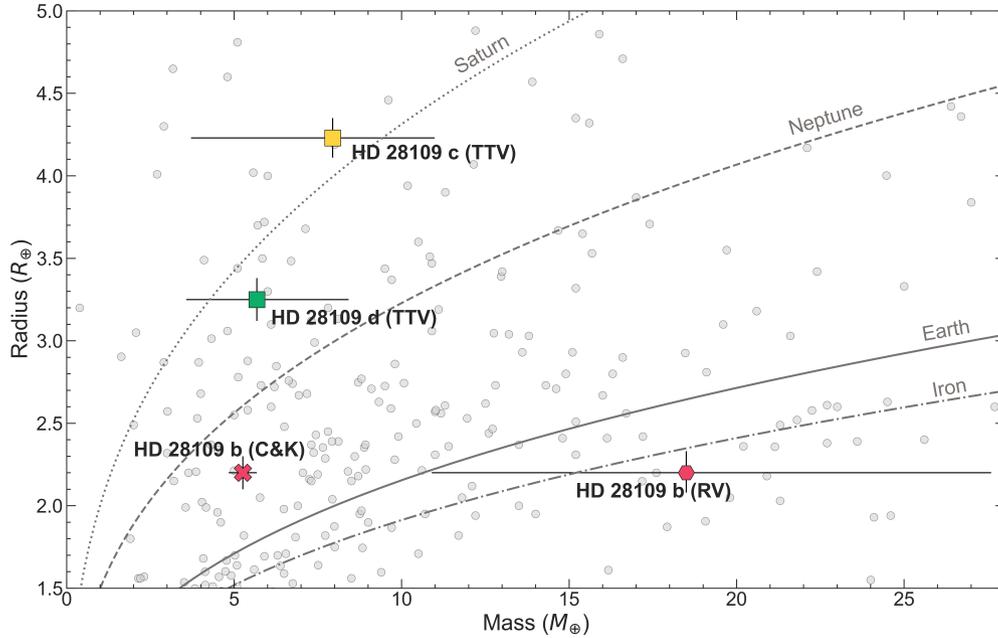
Figure 13. Mass-radius diagram showing the positions of HD 28109 b, c and d. Planets c and d are plotted as squares with their masses are estimated from TTVs. As the mass of planet b is still poorly constrained, we plot its position using its RV estimated mass as a hexagon, while the average mass for planets of its radius (estimated mass following Chen & Kipping (2017)) is plotted as a cross.

are 20, 64, and 38 respectively, while the ESMs are 1.08, 1.43 and 0.52. Given the brightness of the host and the long periods of the planets leading to equilibrium temperatures below 900K, the secondary eclipses would have very low SNR, making characterisation with this method too challenging. However, their TSMs indicate that characterisation with transmission spectroscopy is possible in principle.

We produced model transmission spectra for all three planets using Exo_Transmit (Kempton et al. 2017) assuming solar metallicity and C/O ratio for the host, and cloud-free H_2 dominated atmospheres for the planets. Using these spectra we then used PandExo (Batalha et al. 2017) to simulate Hubble Space Telescope (*HST* hereafter) observations of their atmospheres using transmission spectroscopy. Our simulations indicate that for the two outermost planets a single *HST* transit would be sufficient to carry out reconnaissance spectroscopy (as in de Wit et al. 2018, 2016), to assess the presence of clouds in their atmospheres. In the event of a cloud-free atmosphere, we could detect the presence of water in transmission to 8σ and 3.5σ respectively. To reach a 3.5σ detection for planet b could require a large number of transits, but with its mass unconstrained for the time being we cannot make a fair estimate. As an example, should the mass be consistent with the Chen & Kipping (2017) estimate, we would require 6 transits, each spanning 8 orbits of *HST* to reach a 3.5σ detection. We present the model spectra along with simulated *HST* observations in Figure 14.

We do also note that the simulations described above assume the TTV masses for planets c and d, and the mass estimated from mass-radius relations for planet b. Should any mass be significantly larger the scale height of the atmosphere will decrease, leading to lower significance detections.

7 CONCLUSIONS

In this work we have presented the discovery and confirmation of three sub-Neptune sized planets orbiting HD 28109. Given the brightness of the host, the planets are well-suited to precise radial velocity measurements, which will allow comparison of TTV masses with RV masses. This system is also the brightest *TESS* system discovered to date known to host TTV, making it an exquisite laboratory for planet formation theory. Additionally, we have shown that the outer two planets are well suited to atmospheric reconnaissance with current instrumentation, and they will be high-priority planets for follow-up with *JWST* and *Ariel*.

This work has also demonstrated the capabilities of *ASTEP* as a observatory specialising in planets with long periods, very long transits, and large TTVs. The uninterrupted night enjoyed from Antarctica during two months of the year enables observations of systems that cannot be feasibly followed from anywhere else in the world. Continued selection of these candidates for follow-up will help the community fill out the most sparsely populated parameter spaces in the ever-growing field of exoplanets.
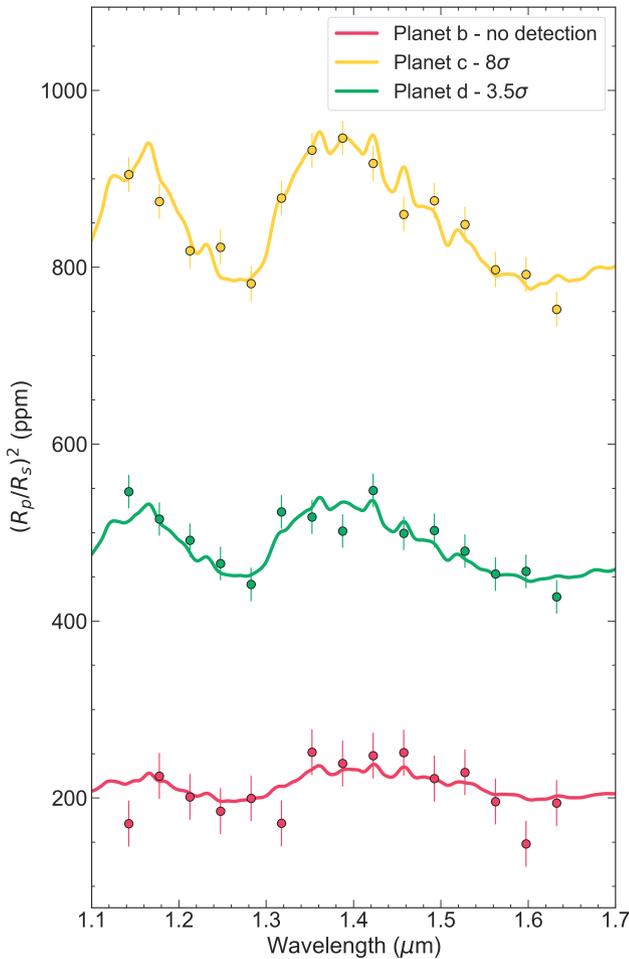
Figure 14. Model transmission spectra of HD 28109 b, c and d with simulated *HST* observations. Each point corresponds to a single transit depth with no offset; the curves represent the simulated transmission spectra.

DATA AVAILABILITY

REFERENCES

Abe L., et al., 2013, A&A, 553, A49
Agol E., Steffen J., Sari R., Clarkson W., 2005, MNRAS, 359, 567
Akeson R. L., et al., 2013, PASP, 125, 989
Aller A., Lillo-Box J., Jones D., Miranda L. F., Barceló Forteza S., 2020, A&A, 635, A128
Astropy Collaboration et al., 2013, A&A, 558, A33
Astropy Collaboration et al., 2018, AJ, 156, 123
Bailer-Jones C. A. L., Rybizki J., Fouesneau M., Demleitner M., Andrae R., 2021, AJ, 161, 147
Baranne A., et al., 1996, A&AS, 119, 373
Batalha N. E., et al., 2017, PASP, 129, 064501
Bean J. L., Raymond S. N., Owen J. E., 2021, Journal of Geophysical Research (Planets), 126, e06639
Borucki W. J., et al., 2010, Science, 327, 977
Brasseur C. E., Phillip C., Fleming S. W., Mullally S. E., White R. L., 2019, Astrocut: Tools for creating cutouts of TESS images (ascl:1905.007)
Broeg C., et al., 2013, in European Physical Journal Web of Conferences. p. 03005 (arXiv:1305.2270), doi:10.1051/epjconf/20134703005
Brown T. M., et al., 2013, Publications of the Astronomical Society of the Pacific, 125, 1031
Buchhave L. A., et al., 2012, Nature, 486, 375
Chen J., Kipping D., 2017, ApJ, 834, 17
Ciardi D. R., Beichman C. A., Horch E. P., Howell S. B., 2015, ApJ, 805, 16
Cincotta P. M., Simó C., 2000, A&AS, 147, 205

Coleman G. A. L., Nelson R. P., 2016, MNRAS, 457, 2480

Collins K. A., Kielkopf J. F., Stassun K. G., Hessman F. V., 2017, AJ, 153, 77

Crouzet N., et al., 2010a, in Spinoglio L., Epchtein N., eds, EAS Publications Series Vol. 40, EAS Publications Series. pp 367–373 (arXiv:1002.2898), doi:10.1051/eas/1040051

Crouzet N., et al., 2010b, A&A, 511, A36

Crouzet N., et al., 2018, A&A, 619, A116

Cutri R. M., et al., 2003, VizieR Online Data Catalog, p. II/246

Dawson R. I., et al., 2021, AJ, 161, 161

Deck K. M., Agol E., 2015, ApJ, 802, 116

Demory B. O., et al., 2020, A&A, 642, A49

Dietrich J., Apai D., 2020, AJ, 160, 107

Donati J. F., Semel M., Carter B. D., Rees D. E., Collier Cameron A., 1997, MNRAS, 291, 658

Eisner N., Lintott C., Aigrain S., 2020, The Journal of Open Source Software, 5, 2101

Fabrycky D. C., et al., 2014, ApJ, 790, 146

Feroz F., Hobson M. P., 2008, MNRAS, 384, 449

Findeisen K., Hillenbrand L., Soderblom D., 2011, AJ, 142, 23

Foreman-Mackey D., Hogg D. W., Lang D., Goodman J., 2013, PASP, 125, 306

Foreman-Mackey D., Agol E., Ambikasaran S., Angus R., 2017, celerite: Scalable 1D Gaussian Processes in C++, Python, and Julia (ascl:1709.008)

Fressin F., et al., 2013, ApJ, 766, 81

Fulton B. J., et al., 2017, AJ, 154, 109

Furlan E., Howell S. B., 2017, AJ, 154, 66

Gaia Collaboration et al., 2016, A&A, 595, A1

Gaia Collaboration et al., 2018, A&A, 616, A1

Gaia Collaboration et al., 2021, A&A, 649, A1

Giacalone S., et al., 2021, AJ, 161, 24

Ginsburg A., et al., 2019, AJ, 157, 98

Ginzburg S., Schlichting H. E., Sari R., 2018, MNRAS, 476, 759

Gray D. F., 2005, The Observation and Analysis of Stellar Photospheres. Cambridge University Press

Guerrero N. M., et al., 2021, ApJS, 254, 39

Guillot T., Santos N. C., Pont F., Iro N., Melo C., Ribas I., 2006, A&A, 453, L21

Guillot T., et al., 2015, Astronomische Nachrichten, 336, 638

Günther M. N., Daylan T., 2019, allesfitter: Flexible star and exoplanet inference from photometry and radial velocity (ascl:1903.003)

Günther M. N., Daylan T., 2021, ApJS, 254, 13

Gupta A., Schlichting H. E., 2020, MNRAS, 493, 792

Hadden S., Barclay T., Payne M. J., Holman M. J., 2019, AJ, 158, 146

Hippke M., Heller R., 2019, TLS: Transit Least Squares (ascl:1910.007)

Hippke M., David T. J., Mulders G. D., Heller R., 2019, AJ, 158, 143

Høg E., et al., 2000, A&A, 355, L27

Holman M. J., Murray N. W., 2005, Science, 307, 1288

Holman M. J., et al., 2010, Science, 330, 51

Houk N., Cowley A. P., 1975, University of Michigan Catalogue of two-dimensional spectral types for the HD stars. Volume I. Declinations -90_ to -53_f0.

Howard A. W., et al., 2010a, Science, 330, 653

Howard A. W., et al., 2010b, ApJ, 721, 1467

Howell S. B., Everett M. E., Sherry W., Horch E., Ciardi D. R., 2011, AJ, 142, 19

Howell S. B., Matson R. A., Ciardi D. R., Everett M. E., Livingston J. H., Scott N. J., Horch E. P., Winn J. N., 2021, AJ, 161, 164

Husser T. O., Wende-von Berg S., Dreizler S., Homeier D., Reiners A., Barman T., Hauschildt P. H., 2013, A&A, 553, A6

Izidoro A., Bitsch B., Raymond S. N., Johansen A., Morbidelli A., Lambrechts M., Jacobson S. A., 2021, A&A, 650, A152

Jenkins J. M., et al., 2016, in Chiozzi G., Guzman J. C., eds, Society of Photo-Optical Instrumentation Engineers (SPIE) Conference Series Vol. 9913, Software and Cyberinfrastructure for Astronomy IV. p. 99133E, doi:10.1117/12.2233418

Jensen E., 2013, Tapir: A web interface for transit/eclipse observability (ascl:1306.007)

Jin S., Mordasini C., 2018, ApJ, 853, 163

Johansen A., Lambrechts M., 2017, Annual Review of Earth and Planetary Sciences, 45, 359

Kass R. E., Raftery A. E., 1995, Journal of the American Statistical Association, 90, 773

Kempton E. M. R., Lupu R., Owusu-Asare A., Slough P., Cale B., 2017, PASP, 129, 044402

Kempton E. M. R., et al., 2018, PASP, 130, 114401

Kipping D. M., 2013, MNRAS, 435, 2152

Kipping D. M., 2014, MNRAS, 440, 2164

Kurucz R. L., 1979, ApJS, 40, 1

Lambrechts M., Morbidelli A., Jacobson S. A., Johansen A., Bitsch B., Izidoro A., Raymond S. N., 2019, A&A, 627, A83

Lee E. J., Chiang E., 2015, ApJ, 811, 41

Lee E. J., Chiang E., 2016, ApJ, 817, 90

Lenzen R., et al., 2003, in Iye M., Moorwood A. F. M., eds, Society of Photo-Optical Instrumentation Engineers (SPIE) Conference Series Vol. 4841, Instrument Design and Performance for Optical/Infrared Ground-based Telescopes. pp 944–952, doi:10.1117/12.460044

Lightkurve Collaboration et al., 2018, Lightkurve: Kepler and TESS time series analysis in Python, Astrophysics Source Code Library (ascl:1812.013)

Lissauer J. J., et al., 2012, ApJ, 750, 112

Lithwick Y., Xie J., Wu Y., 2012, ApJ, 761, 122

Lovis C., Pepe F., 2007, A&A, 468, 1115

Mamajek E. E., Hillenbrand L. A., 2008, ApJ, 687, 1264

Matson R. A., Howell S. B., Horch E. P., Everett M. E., 2018, AJ, 156, 31

Matsumura S., Thommes E. W., Chatterjee S., Rasio F. A., 2010, ApJ, 714, 194

Maxted P. F. L., 2016, A&A, 591, A111

Mayor M., et al., 2003, The Messenger, 114, 20

Mayor M., et al., 2011, arXiv e-prints, p. arXiv:1109.2497

McCully C., Volgenau N. H., Harbeck D.-R., Lister T. A., Saunders E. S., Turner M. L., Siiverd R. J., Bowman M., 2018, in Proc. SPIE. p. 107070K (arXiv:1811.04163), doi:10.1117/12.2314340

Mékarnia D., et al., 2016, MNRAS, 463, 45

Millholland S., 2019, ApJ, 886, 72

Nesvorný D., Vokrouhlický D., 2016, ApJ, 823, 72

Nesvorný D., Kipping D. M., Buchhave L. A., Bakos G. Á., Hartman J., Schmitt A. R., 2012, Science, 336, 1133

Nesvorný D., Kipping D., Terrell D., Hartman J., Bakos G. Á., Buchhave L. A., 2013, ApJ, 777, 3

Nesvorny D., Chrenko O., Flock M., 2021, arXiv e-prints, p. arXiv:2110.09577

Owen J. E., Wu Y., 2013, ApJ, 775, 105

Paredes L. A., Henry T. J., Quinn S. N., Gies D. R., Hinojosa-Goñi R., James H.-S., Jao W.-C., White R. J., 2021, AJ, 162, 176

Parviainen H., Aigrain S., 2015, MNRAS, 453, 3821

Pearson K. A., 2019, AJ, 158, 243

Pepe F., Mayor M., Galland F., Naef D., Queloz D., Santos N. C., Udry S., Burnet M., 2002, A&A, 388, 632

Pepe F., et al., 2021, A&A, 645, A96

Pozuelos F. J., et al., 2020, A&A, 641, A23

Pu B., Wu Y., 2015, ApJ, 807, 44

Rein H., 2012, MNRAS, 427, L21

Rein H., Liu S. F., 2012, A&A, 537, A128

Rein H., Tamayo D., 2015, MNRAS, 452, 376

Ricker G. R., et al., 2015, Journal of Astronomical Telescopes, Instruments, and Systems, 1, 014003

Rousset G., et al., 2003, in Wizinowich P. L., Bonaccini D., eds, Society of Photo-Optical Instrumentation Engineers (SPIE) Conference Series Vol. 4839, Adaptive Optical System Technologies II. pp 140–149, doi:10.1117/12.459332

Savitzky A., Golay M. J. E., 1964, Analytical Chemistry, 36, 1627

Schlegel D. J., Finkbeiner D. P., Davis M., 1998, ApJ, 500, 525

Seager S., Mallén-Ornelas G., 2003, ApJ, 585, 1038

Skilling J., 2004, in Fischer R., Preuss R., Toussaint U. V., eds, American Institute of Physics Conference Series Vol. 735, Bayesian Inference and Maximum Entropy Methods in Science and Engineering: 24th International Workshop on Bayesian Inference and Maximum Entropy Methods in Science and Engineering. pp 395–405, doi:10.1063/1.1835238

Speagle J. S., 2020, MNRAS, 493, 3132

Stassun K. G., Torres G., 2016, AJ, 152, 180

Stassun K. G., Torres G., 2021, ApJ, 907, L33

Stassun K. G., Collins K. A., Gaudi B. S., 2017, AJ, 153, 136

Stassun K. G., Corsaro E., Pepper J. A., Gaudi B. S., 2018, AJ, 155, 22

Stassun K. G., et al., 2019, AJ, 158, 138

Tokovinin A., 2018, PASP, 130, 035002

Tokovinin A., Fischer D. A., Bonati M., Giguere M. J., Moore P., Schwab C., Spronck J. F. P., Szymkowiak A., 2013, PASP, 125, 1336

Torres G., Andersen J., Giménez A., 2010, A&ARv, 18, 67

Twicken J. D., et al., 2018, PASP, 130, 064502

Valencia D., Ikoma M., Guillot T., Nettelmann N., 2010, A&A, 516, A20

Van Eylen V., Agentoft C., Lundkvist M. S., Kjeldsen H., Owen J. E., Fulton B. J., Petigura E., Snellen I., 2018, MNRAS, 479, 4786

Wright E. L., et al., 2010, AJ, 140, 1868

York D. G., et al., 2000, AJ, 120, 1579

Zhou G., et al., 2018, AJ, 156, 93

Ziegler C., Tokovinin A., Briceño C., Mang J., Law N., Mann A. W., 2020, AJ, 159, 19

de Wit J., et al., 2016, Nature, 537, 69

de Wit J., et al., 2018, Nature Astronomy, 2, 214

This paper has been typeset from a TeX/LaTeX file prepared by the author.